Title	Topology optimization for particle flow problems using Eulerian-Eulerian model with a finite difference method
Author(s)	Chen, Chih Hsiang; Yaji, Kentaro
Citation	Computers and Fluids. 2025, 291, p. 106573
Version Type	VoR
URL	https://hdl.handle.net/11094/100983
rights	This article is licensed under a Creative Commons Attribution 4.0 International License.
Note	

Computers and Fluids 291 (2025) 106573

Contents lists available at ScienceDirect

Computers and Fluids

journal homepage: www.elsevier.com/locate/compfluid

Topology optimization for particle flow problems using Eulerian-Eulerian model with a finite difference method

Chih-Hsiang Chen, Kentaro Yaji *

Department of Mechanical Engineering, Graduate School of Engineering, Osaka University, 2-1, Yamadaoka, Suita, Osaka, 565-0871, Japan

ARTICLE INFO

Keywords:
Topology optimization
Particle flow
Eulerian–Eulerian model
Finite difference method

ABSTRACT

Particle flow processing is widely employed across various industrial applications and technologies. Due to the complex interactions between particles and fluids, designing effective devices for particle flow processing is challenging. In this study, we propose a topology optimization method to design flow fields that effectively enhance the resistance encountered by particles. Particle flow is simulated using an Eulerian–Eulerian model based on a finite difference method. Automatic differentiation is implemented to compute sensitivities using a checkpointing algorithm. We formulate the optimization problem as maximizing the variation of drag force on particles while reducing fluid power dissipation. Initially, we validate the finite difference flow solver through numerical examples of particle flow problems and confirm that the corresponding topology optimization produces a result comparable to the benchmark problem. In the optimization cases, we explore both symmetric and asymmetric flow scenarios. For the symmetric flow case, the optimized flow fields indicate that serpentine flow fields can enhance particle drag variation while accounting for power dissipation. Furthermore, we investigate the effects of Reynolds numbers ($Re \leq 100$) and Stokes numbers ($St < 1$) on the optimized flow field. The results demonstrate that increasing the Reynolds number results in more bends and greater curvature in the flow field, whereas increasing the Stokes number reduces these features. For the asymmetric flow case, gravity influences particle distribution, leading the serpentine flow paths to adjust their overall orientation to align with these regions of higher particle concentration.

1. Introduction

The process of handling particle flow plays a pivotal role in a wide range of industrial applications [1,2]. Among the factors governing these processes, the particle residence time—the duration particles spend in a specific region—serves as a fundamental factor of process efficiency, affecting the degree of reaction [3,4], mixing quality [5,6], and heat transfer effect [7,8] in industrial devices. A fundamental approach to adjusting particle residence time is to modify the resistance acting on the particles. This can be achieved by controlling operational conditions [9,10], altering particle properties [11–13], or designing flow paths to impose different levels of resistance [14–16]. Furthermore, it is beneficial to increase the resistance encountered by particles for applications that require extending particle residence time. For instance, in fluidized beds, baffles are used to control particle movement by reducing back-mixing and redistributing particles, which increases resistance and enhances mixing efficiency [17–19]. In microreactors, complex channel designs are employed to extend flow paths and ensure complete chemical reactions [20–22]. Additionally, porous media are incorporated within particle heating receivers to increase the resistance to particle flow, allowing the particles to absorb solar energy effectively and thereby improving thermal efficiency [23,24]. However, the complex interactions between particles and fluid make it challenging to design an effective flow path to increase particle flow resistance. Although size optimization is commonly employed for such requirements [25], predefined shapes offer limited flexibility in determining optimized configurations at the conceptual design stage.

Unlike size and shape optimization, topology optimization can generate optimized configurations without the designer's intuition at the conceptual design stage. The homogenization design method for topology optimization, first proposed by Bendsøe and Kikuchi, processes heterogeneous materials into homogeneous forms to achieve optimized material distribution for enhanced structural performance [26]. Moreover, the density approach, also known as the SIMP (Solid Isotropic Material with Penalization) method, employs a continuous function to enable a smooth transition of design variables throughout the entire design domain in the optimization process [27]. The use of a penalization factor in the SIMP method eliminates intermediate values of design

---

* Corresponding author.
E-mail address: yaji@mech.eng.osaka-u.ac.jp (K. Yaji).

https://doi.org/10.1016/j.compfluid.2025.106573
Received 10 October 2024; Received in revised form 21 January 2025; Accepted 8 February 2025

Nomenclature

$\mathbf{g}$	Gravity Constant ($\mathrm{m/s^2}$)
$\mathbf{n}$	Normal Vector
$\mathbf{u}$	Velocity vector (m/s)
$\mathbf{x}$	Position vector (m)
$\mathscr{D}$	Design domain
τ_p	Particle relaxation time (s)
a	Coefficient of the discretized momentum equations in Eqs. (29) and (30)
b	Coefficient of the pressure-linked equation in Eq. (44)
C_d	Drag coefficient
D	Drag force magnitude (N)
d_p	Particle diameter (m)
H	Pipe height (m)
i, j	Indices of the grid point in Fig. 2
J	Objective function
K	Momentum exchange coefficient ($\mathrm{kg/(m^3\ s)}$)
k	Number of flow simulation iterations
L	Inlet length (m)
l	Phase indicator
l_o	Characteristic length for the obstacle (m)
n	Number of optimization iterations
p	Pressure (Pa)
q	Convex parameter
R	Filter radius (m)
Re	Reynolds number
s	Source term
St	Stokes number
t	Time (s)
U	Characteristic velocity (m/s)
V	Volume constraint
x, y	Coordinates (m)
z	Parameter of the weighting function in Eq. (32)
tol	Convergence tolerance for flow simulation

Greek symbols

α	Inverse permeability ($\mathrm{kg/(m^3\ s)}$)
β	Projection parameter
Δ	Finite difference quantity
ϵ	Convergence tolerance for optimization
η	Threshold parameter
Γ	Boundary of the analysis domain
γ	Design variable
$\hat{\varepsilon}$	Pseudo-dilation defined in Eq. (42)
κ	Pressure conductivity
μ	Viscosity (Pa s)
Ω	Fluid domain
ω	Relaxation factor
$\boldsymbol{\Phi}$	Power dissipation (W/m)
ϕ	Volume fraction
ρ	Density ($\mathrm{kg/m^3}$)
ζ	Drag force variation ($\mathrm{N\ m^2}$)

Subscripts

0	Quantity at the previous time $t - \Delta t$
ave	Average
f	Fluid phase
P	Node notation for point P in Fig. 2
p	Particle phase
W, E, S, N	Neighborhood points of point P
w, e, s, n	Midpoint of each adjacent interval of point P

Superscripts

in	Inlet
out	Outlet
wall	Wall

variables, improving material distribution from a manufacturing viewpoint.

Based on the SIMP method, topology optimization for Stokes flow was pioneered by Borrvall and Petersson [28]. They introduced a fictitious force term to model porous domains, allowing for no-slip boundary conditions by setting a sufficiently high value of fictitious force. Subsequent research has broadened the scope of topology optimization in fluid dynamics. For instance, Guest et al. developed a methodology for optimizing creeping flow conditions [29]. Gersborg-Hansen et al. proposed a topology optimization method for laminar channel flow problems utilizing Navier–Stokes equations [30]. Topology optimization methods for unsteady flow problems have been extended by Kreissl et al. [31] and Deng et al. [32]. Owing to the high degree of design freedom, research in fluid topology optimization is not only limited to pure fluid issues but also includes a wide range of studies that consider interactions with various physical fields [33–37].

In the case of multi-physics problems, there has been growing interest in the topology optimization of particle flows in recent years. Andreasen proposed a topology optimization approach for optimizing inertial microfluidic devices for particle manipulation [38]. Yoon proposed studies focused on controlling particle trajectories in fluid [39–41]. These studies employ the Eulerian–Lagrangian model to explore the topology optimization of single or multiple particles in fluids. It is crucial to highlight that particle modeling can be conducted using either the Eulerian–Lagrangian approach or the Eulerian–Eulerian approach, each offering distinct advantages for particle flow analysis. In the Eulerian–Lagrangian approach, the fluid is treated as a continuum, and each particle is tracked individually within the Lagrangian framework, enabling the detailed simulation of particle trajectories and interactions with the fluid phase [42]. Conversely, the Eulerian–Eulerian approach treats both the gas and particles as continuous phases with their conservation equations, allowing for the investigation of behaviors of numerous particles, including sedimentation, fluidization, and particle residence time distribution [43–45]. Although prior studies have utilized the Eulerian–Lagrangian approach to optimize particle manipulations and trajectory problems, employing the Eulerian–Lagrangian approach to simulate the collective behavior of particles can lead to high consumption of computational resources due to the necessity of tracking each particle individually [46]. Therefore, the Eulerian–Eulerian approach is an efficient choice for problems involving the collective behavior of numerous particles, especially in industrial scenarios requiring computational efficiency and scalability.

On the other hand, according to the literature review [47], most studies on topology optimization employ the finite element method, while a few studies utilize the finite volume method [48], lattice Boltzmann method [49] and particle-based method [50]. Although the finite element method is well-suited for structural problems with arbitrary shapes of objects, it requires relatively significant memory resources [51] and involves specific treatments for conservation law in fluid problems [52,53]. Despite its challenges with complex geometries, the finite difference method effectively handles fluid simulation [54,55] and supports high-order schemes for complex fluid behavior [56,57]. From the view of standard topology optimization methods, an optimized structure is typically determined by the distribution of design variables. There is no need to employ unstructured meshes to address issues of arbitrary structural shapes, which makes the finite difference method an appropriate choice for fluid topology optimization.

In this paper, we propose a topology optimization method for particle flow that aims to enhance the resistance acting on particles while accounting for fluid power dissipation. For the numerical model, we employ a finite difference method and the Eulerian–Eulerian approach to simulate particle flow behaviors. The finite difference scheme called the NAPPLE (Nonstaggered Artificial Pressure for Pressure-Linked Equation) algorithm is selected as our flow solver. The characteristic of the NAPPLE algorithm lies in its use of specific assumptions that allow all state variables to be defined on a collocated grid, thereby simplifying programming and enhancing computational efficiency [58]. In solving optimization problems, GCMMA (Globally Convergent Method of Moving Asymptotes) [59] is widely used for topology optimization and is capable of addressing three-dimensional computations [60–62]. Given its proven efficiency and robustness, we have selected GCMMA to solve the optimization problem in this study. The sensitivity information is computed with automatic differentiation, and a checkpointing algorithm is utilized to reduce memory requirements [63,64]. In the optimization cases, we examine the effects of Reynolds and Stokes numbers on the optimized flow field under symmetric conditions and how asymmetric flow conditions affect the optimization results.

To the best of our knowledge, this is the first topology optimization method to utilize the Eulerian–Eulerian model for handling the collective behavior of particles, specifically aiming to maximize particle drag variation. Additionally, it explores the feasibility of integrating the finite difference method, thereby addressing a critical gap in the field of fluid topology optimization. The subsequent sections of this paper are arranged as follows: In Section 2, we define the governing equations and boundary conditions. In Section 3, we detail the approach for topology optimization and present a problem designed to maximize changes in particle drag force. In Section 4, we first describe the NAPPLE algorithm in detail, followed by the demonstration of the overall numerical implementation, which includes sensitivity calculation and the optimization algorithm. In Section 5, some numerical results are discussed to confirm the efficacy of this proposed method. Finally, the summarization and future work are provided in Section 6.

2. Mathematical model

2.1. Assumption

The interactions between each phase play an important role in particle flow behavior. In the condition of low particle volume fraction, the effect of particles on the fluid is negligible, a concept known as one-way coupling. With the increases in the particle volume fraction, the effect of two-way coupling should be considered for flow characteristics, which means the fluid and particles mutually influence each other. When the volume fraction of particles exceeds 0.1, the particle flow is regarded as dense particle flow, where the particle–particle interactions need to be taken into account [65].

The assumption of one-way coupling is suitable for applications with dilute particles, such as microfluidic devices [66–68]. Accordingly, we adopt one-way coupling under sufficiently dilute conditions, ensuring that properties like particle shape, elasticity, and roughness do not affect the flow field or induce particle–particle interactions. Furthermore, due to the complex interactions between turbulence and particles, and the widespread applications of particle flows in laminar regimes [69], this study focuses on steady-state laminar flow. In this regime, the orientation of particles remains relatively stable, and the particle roughness is negligible because disturbances caused by roughness are minimal under viscous-dominated conditions. Hence, the effect of particle shape and roughness is further diminished. The assumptions for preliminary exploration are outlined below:

- The fluid phase is treated as a steady incompressible laminar flow.
- Due to the dilute condition of the particles, the influence of particles on the fluid and the interactions between particles are not considered.
- The particles are smooth spheres, and the effects of particle shape and roughness are neglected.
- The particles are treated as rigid bodies, and their elasticity is neglected.
- Since the lift force on particles has a minor effect in the investigated cases, the particle lift force is negligible [70].

2.2. Governing equations

We adopt the Eulerian–Eulerian model as our core approach for the numerical investigation. Both phases are formulated by the conservation equations for continuity and momentum. The governing equations for the fluid phase are defined as follows:

$$\nabla \cdot (\phi_\mathrm{f} \rho_\mathrm{f} \mathbf{u}_\mathrm{f} \mathbf{u}_\mathrm{f}) = -\phi_\mathrm{f} \nabla p + \nabla \cdot (\mu \phi_\mathrm{f} (\nabla \mathbf{u}_\mathrm{f} + \nabla \mathbf{u}_\mathrm{f}^\mathrm{T})) + \phi_\mathrm{f} \rho_\mathrm{f} \mathbf{g}, \tag{1}$$

$$\nabla \cdot (\phi_\mathrm{f} \mathbf{u}_\mathrm{f}) = 0, \tag{2}$$

where ϕ_f is the fluid volume fraction, ρ_f is the fluid density, μ is the fluid viscosity, $\mathbf{g}$ is the gravity constant, p is the pressure, and $\mathbf{u}_\mathrm{f}$ is the velocity vector of fluid phase. Similarly, the governing equations for the particle phase in the Eulerian–Eulerian formulation are defined as follows:

$$\nabla \cdot (\phi_\mathrm{p} \rho_\mathrm{p} \mathbf{u}_\mathrm{p} \mathbf{u}_\mathrm{p}) = -\phi_\mathrm{p} \nabla p + \phi_\mathrm{p} \rho_\mathrm{p} \mathbf{g} + K(\mathbf{u}_\mathrm{f} - \mathbf{u}_\mathrm{p}), \tag{3}$$

$$\nabla \cdot (\phi_\mathrm{p} \mathbf{u}_\mathrm{p}) = 0, \tag{4}$$

where $\mathbf{u}_\mathrm{p}$ is the velocity vector of particle phase, ϕ_p is the particle volume fraction, ρ_p is the particle density, K is the interphase momentum exchange coefficient. To consider the momentum exchange between the fluid phase and the particle phase, the source term related to the momentum exchange coefficient K is incorporated into the momentum equation for the particle phase, which can be determined by the Gidaspow model [71] expressed as follows:

$$K = \begin{cases} \dfrac{3}{4} C_\mathrm{d} \dfrac{\phi_\mathrm{p} \phi_\mathrm{f} \rho_\mathrm{f} |\mathbf{u}_\mathrm{f} - \mathbf{u}_\mathrm{p}|}{d_\mathrm{p}} \phi_\mathrm{f}^{-2.65}, & \text{if } \phi_\mathrm{f} > 0.8 \\ 150 \dfrac{\phi_\mathrm{p}^2 \mu_\mathrm{f}}{\phi_\mathrm{f} d_\mathrm{p}^2} + 1.75 \dfrac{\phi_\mathrm{p} \rho_\mathrm{f} |\mathbf{u}_\mathrm{f} - \mathbf{u}_\mathrm{p}|}{d_\mathrm{p}}, & \text{if } \phi_\mathrm{f} \le 0.8, \end{cases} \tag{5}$$

where d_p is the particle diameter, and C_d is the drag coefficient, which is defined by Kolve [71] as follows:

$$C_\mathrm{d} = \begin{cases} \dfrac{24}{Re_\mathrm{p}}, & \text{if } Re_\mathrm{p} < 1 \\ \dfrac{24}{Re_\mathrm{p}} (1 + 0.15 Re_\mathrm{p}^{0.687}), & \text{if } 1 \le Re_\mathrm{p} \le 1000, \end{cases} \tag{6}$$

where Re_p is the particle Reynolds number, which can be described as:

$$Re_\mathrm{p} = \frac{\rho_\mathrm{f} |\mathbf{u}_\mathrm{f} - \mathbf{u}_\mathrm{p}| d_\mathrm{p}}{\mu}. \tag{7}$$

In this study, we consider the cases of symmetric and asymmetric flow conditions. Fig. 1 shows the analysis domains and boundary conditions. For momentum conservation, the Dirichlet boundary conditions for velocities of both phases are imposed at the inlet. The Dirichlet

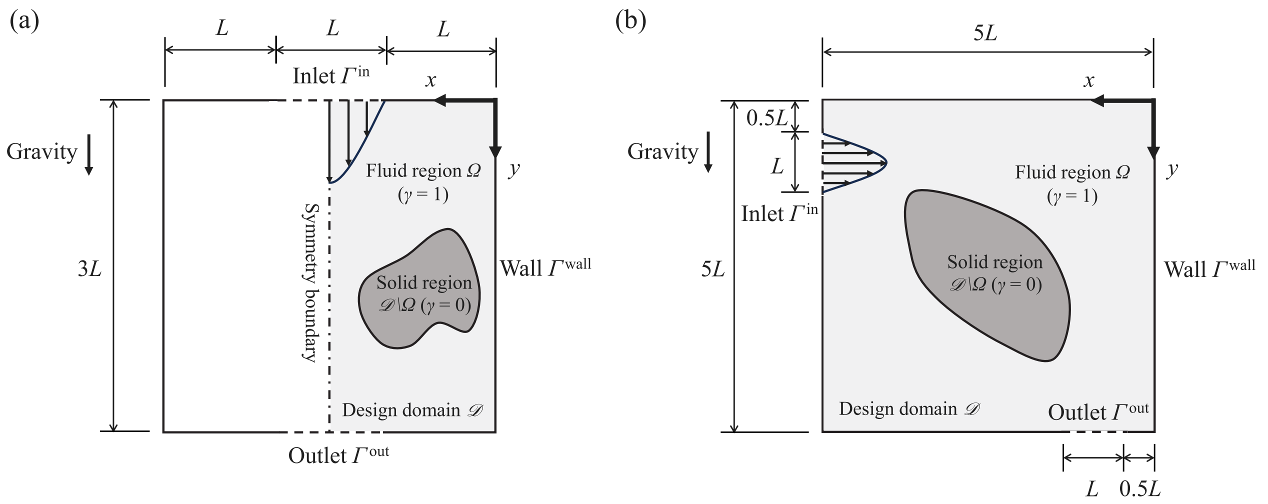

Fig. 1. Schematic diagrams for the analysis domains and boundary conditions: (a) symmetrical flow (b) asymmetrical flow.

boundary condition for pressure is specified at the outlet, and no-slip boundary conditions are applied to the walls. The expressions are shown below:

$$\mathbf{u}_{\mathrm{f}} = \mathbf{u}_{\mathrm{f}}^{\mathrm{in}}, \quad \mathbf{u}_{\mathrm{p}} = \mathbf{u}_{\mathrm{p}}^{\mathrm{in}} \quad \text{on} \quad \Gamma^{\mathrm{in}}, \tag{8}$$

$$\mathbf{u}_{\mathrm{f}} = \mathbf{0}, \quad \mathbf{u}_{\mathrm{p}} = \mathbf{0} \quad \text{on} \quad \Gamma^{\mathrm{wall}}, \tag{9}$$

$$p = p^{\mathrm{out}} \quad \text{on} \quad \Gamma^{\mathrm{out}}, \tag{10}$$

where $\mathbf{u}_{\mathrm{f}}^{\mathrm{in}}$ and $\mathbf{u}_{\mathrm{p}}^{\mathrm{in}}$ are the fluid velocity and particle velocity at the inlet, respectively, and p^{out} is the prescribed value for pressure at the outlet. Besides, for the volume fraction, the Dirichlet boundary condition for the particle phase is also defined on the inlet, and the Neumann boundary condition is specified on the remaining boundaries. The expressions are as follows:

$$\phi_{\mathrm{p}} = \phi_{\mathrm{p}}^{\mathrm{in}}, \quad \text{on} \quad \Gamma^{\mathrm{in}}, \tag{11}$$

$$\nabla\phi_{\mathrm{p}} \cdot \mathbf{n} = 0, \quad \text{on} \quad \Gamma^{\mathrm{wall}}, \Gamma^{\mathrm{out}}, \tag{12}$$

where $\phi_{\mathrm{p}}^{\mathrm{in}}$ is the prescribed value of particle volume fraction at the inlet. Note that since the summation of the volume fraction of both phases is equal to one at any given node, specifying the particle volume fraction on the boundaries automatically determines the fluid volume fraction. Both numerical examples also account for gravity, aligned in the direction of the y-axis.

3. Problem formulation

3.1. Basic concept of topology optimization

Topology optimization aims to derive an optimized design within a design domain $\mathscr{D}$, guided by a specific objective function and constraints. Essentially, the basic idea of topology optimization involves introducing design variables to transform a structural design problem into a material distribution problem. We formulate the expression of design variables as follows:

$$\chi(\mathbf{x}) = \begin{cases} 1, & \text{if } \mathbf{x} \in \Omega \\ 0, & \text{if } \mathbf{x} \in \mathscr{D}\backslash\Omega, \end{cases} \tag{13}$$

where $\mathbf{x}$ is the position in $\mathscr{D}$, and Ω represents the flow domain in $\mathscr{D}$. With the discontinuity of the characteristic function $\chi(\mathbf{x})$, relaxation techniques are commonly employed to achieve a continuous transition for numerical treatment. In this study, a popular method called the density approach is utilized for topology optimization, where the material distribution is defined by a continuous function with values ranging from $0 \leq \gamma(\mathbf{x}) \leq 1$.

To ensure the smoothness of the material layout, we employ convolution filtering [72,73] to prevent the occurrence of checkerboard patterns in material distribution [74], as follows:

$$\tilde{\gamma}_k = \frac{\sum_{i \in N_{e,k}} w(\mathbf{x}_i)\gamma_i}{\sum_{i \in N_{e,k}} w(\mathbf{x}_i)}, \tag{14}$$

where $\tilde{\gamma}_k$ is the filtered design variable on node k, $N_{e,k}$ is the set of nodes within the filtering radius R, and $w(\mathbf{x}_i)$ is the weighting function for filtering defined in the following equation.

$$w(\mathbf{x}_i) = R - |\mathbf{x}_i - \mathbf{x}_k|. \tag{15}$$

Although the filter can ensure a smooth transition of design variables, it also results in more transitional regions with intermediate values between 0 and 1. Therefore, a projection function is used to eliminate transitional grey values, as follows [75]:

$$\bar{\tilde{\gamma}}_k = \frac{\tanh(\beta\eta) + \tanh(\beta(\tilde{\gamma}_k - \eta))}{\tanh(\beta\eta) + \tanh(\beta(1 - \eta))}, \tag{16}$$

where $\bar{\tilde{\gamma}}_k$ is the design variable after projection; β is the projection parameter, which controls the sharpness of contours; and η is the threshold parameter.

3.2. Fluid and solid representation using the design variable field

As mentioned in Section 3.1, we employ a relaxed characteristic function for topology optimization on particle flow. In this study, $\gamma = 1$ represents the fluid region in Ω, and $\gamma = 0$ represents the pseudo-solid region in $\mathscr{D}\backslash\Omega$. To allocate fluid and solid in the design domain, according to the previous research for fluid topology optimization [28], the fictitious body force is required to incorporate into the momentum Eqs. (1) and (3) for both phases, which are re-formulated as follows:

$$\nabla \cdot (\phi_{\mathrm{f}}\rho_{\mathrm{f}}\mathbf{u}_{\mathrm{f}}\mathbf{u}_{\mathrm{f}}) = -\phi_{\mathrm{f}}\nabla p + \nabla \cdot (\mu\phi_{\mathrm{f}}(\nabla\mathbf{u}_{\mathrm{f}} + \nabla\mathbf{u}_{\mathrm{f}}^{\mathrm{T}})) + \phi_{\mathrm{f}}\rho_{\mathrm{f}}\mathbf{g} - \phi_{\mathrm{f}}\alpha_{\mathrm{f}}\mathbf{u}_{\mathrm{f}}, \tag{17}$$

$$\nabla \cdot (\phi_{\mathrm{p}}\rho_{\mathrm{p}}\mathbf{u}_{\mathrm{p}}\mathbf{u}_{\mathrm{p}}) = -\phi_{\mathrm{p}}\nabla p + \phi_{\mathrm{p}}\rho_{\mathrm{p}}\mathbf{g} + K(\mathbf{u}_{\mathrm{f}} - \mathbf{u}_{\mathrm{p}}) - \phi_{\mathrm{p}}\alpha_{\mathrm{p}}\mathbf{u}_{\mathrm{p}}. \tag{18}$$

The inverse permeability α can be expressed as follows:

$$\alpha_l(\bar{\tilde{\gamma}}) = \overline{\alpha}_l + (\underline{\alpha}_l - \overline{\alpha}_l)\bar{\tilde{\gamma}}\frac{1+q}{\bar{\tilde{\gamma}}+q}, \tag{19}$$

where l denotes the phase with $l \in \{\mathrm{f}, \mathrm{p}\}$, $\overline{\alpha}_l$ and $\underline{\alpha}_l$ are the maximum and minimum values of the inverse permeability, respectively, and q is the convex parameter used to control the degree of penalization for intermediate media. It is crucial to note that since the inertia of particles is much greater than that of the fluid, using the same maximum value of the fictitious body force may lead to undesirable penetration of particles into solid regions. To ensure a more realistic simulation, we adjust the maximum fictitious body force for particles as follows, taking into account their greater inertia:

$$\overline{\alpha}_{\mathrm{p}} = c_\alpha \overline{\alpha}_{\mathrm{f}}, \tag{20}$$

where $\overline{\alpha}_{\mathrm{p}}$ is the maximum value of the inverse permeability for the particle phase, $\overline{\alpha}_{\mathrm{f}}$ is the maximum value of the inverse permeability for the fluid phase, and c_α is the coefficient to increase the fictitious body force for the particle phase. Based on a sufficiently large value of the fictitious body force, it is difficult for both phases to pass through the solid region ($\gamma = 0$). Note that though the issue of particle penetration can be addressed by adjusting the maximum value of the fictitious body force, the shear stress exerted by the pseudo-solids on the particles is simplified to no-slip conditions due to a limitation in the mathematical representation of Darcy's force. Despite this simplification, sensitivities can be utilized to obtain the optimized distribution of pseudo-solids using the design variable field.

3.3. Maximization problem: particle drag variation

Under fixed operating conditions, increasing particle resistance is typically achieved through flow field design that either lengthens the particle path or introduces obstacles within the device. Due to the relatively longer relaxation time, particles cannot instantly follow changes in fluid velocity, particularly when encountering obstacles. This results in a velocity difference between the particles and the fluid. Additionally, the continuous changes in the flow path prevent the particles from reaching their terminal velocity, further sustaining the velocity difference. This sustained velocity difference enhances the drag force acting on the particles, as described by the term $K(\mathbf{u}_{\mathrm{f}} - \mathbf{u}_{\mathrm{p}})$ in Eq. (3). As the particles undergo repeated acceleration and deceleration due to obstacles or turns in the flow path, the drag force acting on them varies accordingly. Based on this, the variation in particle drag force can be regarded as a key indicator of the resistance experienced by the particles. Therefore, we formulate a topology optimization problem to maximize the magnitude of particle drag variation, while also considering power dissipation to meet industrial application requirements. The expression of the optimization problem is shown below:

$$\begin{aligned} &\text{maximize } J = w_\zeta \frac{\zeta}{\hat{\zeta}} - w_{\Phi} \frac{\Phi}{\hat{\Phi}}, \\ &\text{subject to } V = \int_\Omega \gamma(\mathbf{x}) d\Omega - \overline{V} \leq 0, \\ &\qquad\qquad 0 \leq \gamma(\mathbf{x}) \leq 1 \text{ for } \forall \mathbf{x} \in \mathscr{D}, \end{aligned} \tag{21}$$

where J is the multi-objective function, w_Φ and w_ζ are the weighting factors, Φ is the power dissipation of the fluid phase, ζ is a function related to the variation of drag force on the particle phase, and $\overline{V}$ is the maximum value of the volume constraint. Due to the difference in scale between Φ and ζ, they are normalized based on their values $\hat{\Phi}$ and $\hat{\zeta}$ from the first iteration of the optimization process. The functions Φ and ζ can be expressed as follows:

$$\Phi = \int_\Omega \left[\frac{1}{2} \mu (\nabla \mathbf{u}_{\mathrm{f}} + \nabla \mathbf{u}_{\mathrm{f}}^{\mathrm{T}}) : (\nabla \mathbf{u}_{\mathrm{f}} + \nabla \mathbf{u}_{\mathrm{f}}^{\mathrm{T}}) + \alpha(\bar{\tilde{\gamma}}) |\mathbf{u}_{\mathrm{f}}|^2 \right] d\Omega, \tag{22}$$

$$\zeta = \int_\Omega (D - \overline{D}) d\Omega, \tag{23}$$

where D represents the magnitude of particle drag force, given by the equation $D = K|\mathbf{u}_{\mathrm{f}} - \mathbf{u}_{\mathrm{p}}|$, and $\overline{D}$ is the average value of particle drag magnitude in Ω.

4. Numerical implementation

4.1. NAPPLE algorithm

The finite difference method called the NAPPLE algorithm [58] is employed for the numerical analysis with in-house C++ code. A distinguishing feature of this algorithm is its ability to define all state variables using a collocated grid system. This approach eliminates the need for a staggered grid to address the checkerboard pressure issue [76,77], which makes programming more straightforward and computation more efficient. In this section, we will introduce the concepts of the NAPPLE algorithm and numerical discretization.

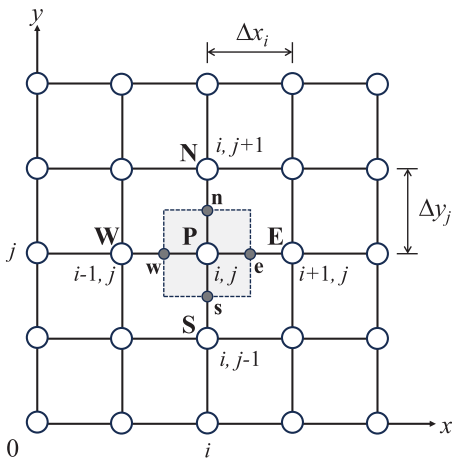

Fig. 2. Node Notation for point **P** on a Cartesian grid system.

We consider a uniform Cartesian grid system for spatial discretization. A point **P** is denoted as P(i, j), where i and j indicate the column number and the row number of point **P** along the x-axis and the y-axis, as shown in Fig. 2. To ensure numerical stability, we use the pseudo-transient method to achieve steady-state solutions [78]. This method introduces a pseudo-time derivative, allowing the changes in state variables to progressively diminish to zero as pseudo-time steps march forward. Therefore, we consider dimensionless transient governing equations for both phases and rewrite Eqs. (1)–(4) under the assumption of incompressible flow as follows:

$$Re\phi_{\mathrm{f}}^* \frac{\partial \mathbf{u}_{\mathrm{f}}^*}{\partial t^*} + Re\phi_{\mathrm{f}}^* (\mathbf{u}_{\mathrm{f}}^* \cdot \nabla^*) \mathbf{u}_{\mathrm{f}}^* = -\phi_{\mathrm{f}}^* \nabla^* \hat{p} + \nabla^* \cdot (\phi_{\mathrm{f}}^* \nabla^* \mathbf{u}_{\mathrm{f}}^*) + \mathbf{s}_{\mathrm{f}}^*, \tag{24}$$

$$\frac{\partial \phi_{\mathrm{f}}^*}{\partial t^*} + \nabla^* \cdot (\phi_{\mathrm{f}}^* \mathbf{u}_{\mathrm{f}}^*) = 0, \tag{25}$$

$$Re\hat{\rho}\phi_{\mathrm{p}}^* \frac{\partial \mathbf{u}_{\mathrm{p}}^*}{\partial t^*} + Re\hat{\rho}\phi_{\mathrm{p}}^* (\mathbf{u}_{\mathrm{p}}^* \cdot \nabla^*) \mathbf{u}_{\mathrm{p}}^* = -\phi_{\mathrm{p}}^* \nabla^* \hat{p} + \mathbf{s}_{\mathrm{p}}^*, \tag{26}$$

$$\frac{\partial \phi_{\mathrm{p}}^*}{\partial t^*} + \nabla^* \cdot (\phi_{\mathrm{p}}^* \mathbf{u}_{\mathrm{p}}^*) = 0, \tag{27}$$

where $\mathbf{s}_{\mathrm{f}}$ is the source term for the fluid phase, given by $\nabla \cdot (\mu \phi_{\mathrm{f}} \nabla \mathbf{u}_{\mathrm{f}}^{\mathrm{T}}) + \phi_{\mathrm{f}} \rho_{\mathrm{f}} \mathbf{g}$, and $\mathbf{s}_{\mathrm{p}}$ is the source term for the particle phase, given by $\phi_{\mathrm{p}} \rho_{\mathrm{p}} \mathbf{g} + K(\mathbf{u}_{\mathrm{f}} - \mathbf{u}_{\mathrm{p}})$. Notably, since the transpose term in the viscous term will be treated explicitly in the discretization procedure, it is included in the source term. The variables with asterisks represent the dimensionless variables defined as follows:

$$\begin{aligned} &\mathbf{u}_{\mathrm{f}}^* = \frac{\mathbf{u}_{\mathrm{f}}}{U}, \ \mathbf{u}_{\mathrm{p}}^* = \frac{\mathbf{u}_{\mathrm{p}}}{U}, \ \phi_{\mathrm{f}}^* = \frac{\phi_{\mathrm{f}}}{\phi}, \ \phi_{\mathrm{p}}^* = \frac{\phi_{\mathrm{p}}}{\phi}, \ \mathbf{s}_{\mathrm{f}}^* = \frac{L^2}{\mu U} \mathbf{s}_{\mathrm{f}}, \ \mathbf{s}_{\mathrm{p}}^* = \frac{L^2}{\mu U} \mathbf{s}_{\mathrm{p}}, \\ &\nabla^* = L\nabla, \ \ t^* = \frac{U}{L} t, \ Re = \frac{\rho U L}{\mu}, \ \ p^* = \frac{p - p_0}{\rho_{\mathrm{f}} U^2}, \ \hat{p} = Rep^*, \ \hat{\rho} = \frac{\rho_{\mathrm{p}}}{\rho_{\mathrm{f}}}, \end{aligned} \tag{28}$$

where U is the characteristic velocity, L is the characteristic length, and Re is the flow Reynolds number. For simplicity, the dimensionless variables used in this section will be written without the asterisk in the following description.

Due to the implicit discretization scheme used in the NAPPLE algorithm, the governing equations are discretized into a matrix of linear algebraic equations to solve for the state variables. For the discretization process, the weighting function scheme [79] is employed for the momentum equations of the fluid phase, and a well-known upwind scheme [54] is utilized for the particle phase to ensure numerical stability. Owing to its general familiarity, the explanation of the upwind scheme employed for the particle phase will not be expanded upon in this section. Instead, we will focus on detailing the weighting function scheme used for the fluid phase. Considering a point P(i, j) on a structured grid shown in Fig. 2, the discretized momentum Eqs. (24) in the x-direction and the y-direction can be expressed as follows:

$$(a_{\mathrm{W}})_{i,j}u_{i-1,j} + (a_{\mathrm{S}})_{i,j}u_{i,j-1} + (a_{\mathrm{P}})_{i,j}u_{i,j} + (a_{\mathrm{E}})_{i,j}u_{i+1,j} + (a_{\mathrm{N}})_{i,j}u_{i,j+1} = (r_u)_{i,j} + \frac{\partial \hat{p}}{\partial x}, \tag{29}$$

$$(a_{\mathrm{W}})_{i,j}v_{i-1,j} + (a_{\mathrm{S}})_{i,j}v_{i,j-1} + (a_{\mathrm{P}})_{i,j}v_{i,j} + (a_{\mathrm{E}})_{i,j}v_{i+1,j} + (a_{\mathrm{N}})_{i,j}v_{i,j+1} = (r_v)_{i,j} + \frac{\partial \hat{p}}{\partial y}, \tag{30}$$

where u is the x-component of velocity, v is the y-component of velocity, a is the weighting coefficient and the subscripts $\mathrm{W}, \mathrm{E}, \mathrm{S}, \mathrm{N}$ denote the neighborhood grid points of point **P** as shown in Fig. 2. The terms r_u and r_v are the remainders in Eqs. (29) and (30). The weighting coefficients can be further expressed with the weighting function scheme as follows:

$$\begin{aligned}
&(a_{\mathrm{W}})_{i,j} = \frac{w_f((z_{\mathrm{w}})_{i,j})}{\Delta x^2}, (a_{\mathrm{E}})_{i,j} = \frac{w_f(-(z_{\mathrm{e}})_{i,j})}{\Delta x^2}, (a_{\mathrm{S}})_{i,j} = \frac{w_f((z_{\mathrm{s}})_{i,j})}{\Delta y^2},\\
&(a_{\mathrm{N}})_{i,j} = \frac{w_f(-(z_{\mathrm{n}})_{i,j})}{\Delta y^2},\\
&(a_{\mathrm{P}})_{i,j} = -(a_{\mathrm{W}})_{i,j} - (a_{\mathrm{S}})_{i,j} - (a_{\mathrm{E}})_{i,j} - (a_{\mathrm{N}})_{i,j} - \frac{Re}{\Delta t},\\
&(r_u)_{i,j} = -\left(\frac{s_x}{\phi} + \frac{Re\ u_0}{\Delta t}\right)_{\mathrm{f}}, \quad (r_v)_{i,j} = -\left(\frac{s_y}{\phi} + \frac{Re\ v_0}{\Delta t}\right)_{\mathrm{f}},
\end{aligned} \tag{31}$$

where the subscript f denotes the fluid phase, the subscripts $\mathrm{w}, \mathrm{e}, \mathrm{s}, \mathrm{n}$ denote the midpoint between each adjacent interval of point **P**, u_0 is the x-component of velocity at the previous time step, and v_0 is the y-component of velocity at the previous time step. The weighting function $w_f(z)$ and the parameter z used in Eq. (31) are defined as follows:

$$\begin{aligned}
&w_f(z) = \frac{z}{1 - e^{-z}},\\
&(z_{\mathrm{w}})_{i,j} = \left(Re\bar{u}_{i-1} - \frac{1}{\bar{\phi}_{i-1}}\frac{\partial \phi}{\partial x}\right)_{\mathrm{f}} \Delta x, \quad (z_{\mathrm{e}})_{i,j} = \left(Re\bar{u}_{i} - \frac{1}{\bar{\phi}_{i}}\frac{\partial \phi}{\partial x}\right)_{\mathrm{f}} \Delta x,\\
&(z_{\mathrm{s}})_{i,j} = \left(Re\bar{v}_{j-1} - \frac{1}{\bar{\phi}_{j-1}}\frac{\partial \phi}{\partial y}\right)_{\mathrm{f}} \Delta y, \quad (z_{\mathrm{n}})_{i,j} = \left(Re\bar{v}_{j} - \frac{1}{\bar{\phi}_{j}}\frac{\partial \phi}{\partial y}\right)_{\mathrm{f}} \Delta y,
\end{aligned} \tag{32}$$

where $\bar{u}_i$, $\bar{v}_j$, $\bar{\phi}_i$ and $\bar{\phi}_j$ represent the average velocity and the average volume fraction in the intervals $x_{i-1} \le x \le x_i$ and $y_{i-1} \le y \le y_i$, respectively. For the weighting function $w_f(z)$ in Eq. (32), we use the power-law approximation to reduce the computational cost [80], given by the equation $w_f(z) \approx [0, (1 - 0.1|z|)^5] + [0, z]$. Besides, as suggested by Lee [81], the unsteady term in Eq. (24) is discretized with implicit form as follows:

$$\frac{\partial \mathbf{u}_{\mathrm{f}}}{\partial t} = \left(\frac{\mathbf{u} - \mathbf{u}_0}{\Delta t}\right)_{\mathrm{f}}. \tag{33}$$

Though Eqs. (29) and (30) are solvable with the initial guess of the pressure field, it is not guaranteed to satisfy the continuity equation. Therefore, it is required to update state variables iteratively, similar to the well-known SIMPLE algorithm [82]. Unlike the SIMPLE algorithm, which relies on a pressure-correction equation, the NAPPLE algorithm integrates the discretized continuity equation and momentum equations to derive a pressure-linked equation. This equation is then directly used to compute the pressure field. To derive the pressure-linked equation, we first recast Eqs. (29) and (30) into a compact form for the volume flux:

$$(\phi_{i,j}u_{i,j})_{\mathrm{f}} = (\phi_{i,j}\hat{u}_{i,j})_{\mathrm{f}} - \kappa_{i,j}\left(\frac{\partial \hat{p}}{\partial x}\right), \tag{34}$$

$$(\phi_{i,j}v_{i,j})_{\mathrm{f}} = (\phi_{i,j}\hat{v}_{i,j})_{\mathrm{f}} - \kappa_{i,j}\left(\frac{\partial \hat{p}}{\partial y}\right), \tag{35}$$

$$\hat{u}_{i,j} = ((r_u)_{i,j} - (a_{\mathrm{W}})_{i,j}u_{i-1,j} - (a_{\mathrm{S}})_{i,j}u_{i,j-1} - (a_{\mathrm{P}})_{i,j}u_{i,j} - (a_{\mathrm{E}})_{i,j}u_{i+1,j} - (a_{\mathrm{N}})_{i,j}u_{i,j+1})/(a_{\mathrm{P}})_{i,j}, \tag{36}$$

$$\hat{v}_{i,j} = ((r_v)_{i,j} - (a_{\mathrm{W}})_{i,j}v_{i-1,j} - (a_{\mathrm{S}})_{i,j}v_{i,j-1} - (a_{\mathrm{P}})_{i,j}v_{i,j} - (a_{\mathrm{E}})_{i,j}v_{i+1,j} - (a_{\mathrm{N}})_{i,j}v_{i,j+1})/(a_{\mathrm{P}})_{i,j}, \tag{37}$$

$$\kappa_{i,j} = -\left(\frac{\phi}{(a_{\mathrm{P}})_{i,j}}\right)_{\mathrm{f}}. \tag{38}$$

As suggested by Moukalled et al. [83], we sum the continuity equations (25) and (27) to obtain the global continuity equation. Subsequently, the global continuity equation can be utilized to derive the pressure-linked equation, thereby solving for the pressure term shared by both phases. The discretized global continuity equation for point P(i, j) can be expressed in the following form:

$$\sum_{l \in \{\mathrm{f,p}\}}\left(\frac{\phi_{i+1,j}u_{i+1,j} - \phi_{i-1,j}u_{i-1,j}}{2\Delta x} + \frac{\phi_{i,j+1}v_{i,j+1} - \phi_{i,j-1}v_{i,j-1}}{2\Delta y}\right)_l = 0. \tag{39}$$

It should be noted that since the sum of the volume fraction of both phases is equal to one at any given time, the influence of the transient term in the global continuity equation can be neglected. Furthermore, as suggested by the prior work [58], we adopted the assumptions shown below during the discretization process:

$$\frac{\kappa_{i+1,j}\left(\frac{\partial \hat{p}}{\partial x}\right)_{i+1,j} - \kappa_{i-1,j}\left(\frac{\partial \hat{p}}{\partial x}\right)_{i-1,j}}{2\Delta x} \approx \frac{\partial}{\partial x}\left(\kappa\frac{\partial \hat{p}}{\partial x}\right), \tag{40}$$

$$\frac{\kappa_{i,j+1}\left(\frac{\partial \hat{p}}{\partial y}\right)_{i,j+1} - \kappa_{i,j-1}\left(\frac{\partial \hat{p}}{\partial y}\right)_{i,j-1}}{2\Delta y} \approx \frac{\partial}{\partial y}\left(\kappa\frac{\partial \hat{p}}{\partial y}\right). \tag{41}$$

Based on the assumptions in Eqs. (40) and (41), integrating Eqs. (34)–(39) yields the pressure-linked equation, which eliminates the checkerboard pressure pattern [58]. The pressure-linked equation is formulated as follows:

$$\frac{\partial}{\partial x}\left(\kappa\frac{\partial \hat{p}}{\partial x}\right) + \frac{\partial}{\partial y}\left(\kappa\frac{\partial \hat{p}}{\partial y}\right) = \hat{\varepsilon}, \tag{42}$$

$$\hat{\varepsilon}_{i,j} = \sum_{l \in \{\mathrm{f,p}\}}\left(\frac{\phi_{i+1,j}\hat{u}_{i+1,j} - \phi_{i-1,j}\hat{u}_{i-1,j}}{2\Delta x} + \frac{\phi_{i,j+1}\hat{v}_{i,j+1} - \phi_{i,j-1}\hat{v}_{i,j-1}}{2\Delta y}\right)_l, \tag{43}$$

where $\hat{\varepsilon}$ is the pseudo-dilation. The pressure-linked equation can also be discretized into a linear algebraic equation with the harmonic scheme [80]:

$$(b_{\mathrm{W}})_{i,j}p_{i-1,j} + (b_{\mathrm{S}})_{i,j}p_{i,j-1} + (b_{\mathrm{P}})_{i,j}p_{i,j} + (b_{\mathrm{E}})_{i,j}p_{i+1,j} + (b_{\mathrm{N}})_{i,j}p_{i,j+1} = (r_p)_{i,j}. \tag{44}$$

The coefficient b in Eq. (44) can be further expressed as follows:

$$\begin{aligned}
&(b_{\mathrm{W}})_{i,j} = \frac{(\kappa_{\mathrm{w}})_{i,j}}{\Delta x^2}, (b_{\mathrm{E}})_{i,j} = \frac{(\kappa_{\mathrm{e}})_{i,j}}{\Delta x^2}, (b_{\mathrm{S}})_{i,j} = \frac{(\kappa_{\mathrm{s}})_{i,j}}{\Delta y^2}, (b_{\mathrm{N}})_{i,j} = \frac{(\kappa_{\mathrm{n}})_{i,j}}{\Delta y^2},\\
&(b_{\mathrm{P}})_{i,j} = -(b_{\mathrm{W}})_{i,j} - (b_{\mathrm{S}})_{i,j} - (b_{\mathrm{E}})_{i,j} - (b_{\mathrm{N}})_{i,j}, \ (r_p)_{i,j} = \hat{\varepsilon}_{i,j},
\end{aligned} \tag{45}$$

Since the global pressure is shared by both the fluid phase and the particle phase, the total pressure conductivity κ represents the sum of the pressure conductivities of each phase. In each phase, the pressure conductivity can be obtained through the coefficients in their respective momentum equations. Therefore, the total pressure conductivity κ can be expressed as follows:

$$\begin{aligned}
(\kappa_{\mathrm{w}})_{i,j} &= \sum_{l \in \{\mathrm{f,p}\}}\left(\frac{2}{(\kappa_{i,j})^{-1} + (\kappa_{i-1,j})^{-1}}\right)_l\\
&= \sum_{l \in \{\mathrm{f,p}\}}\left(\frac{-2\phi_{i,j}\phi_{i-1,j}}{(a_{\mathrm{P}})_{i,j}\phi_{i-1,j} + \phi_{i,j}(a_{\mathrm{P}})_{i-1,j}}\right)_l,\\
(\kappa_{\mathrm{e}})_{i,j} &= \sum_{l \in \{\mathrm{f,p}\}}\left(\frac{2}{(\kappa_{i,j})^{-1} + (\kappa_{i+1,j})^{-1}}\right)_l
\end{aligned} \tag{46}$$

Algorithm 1 NAPPLE algorithm for solving particle flow problem

```
All the state variables and the parameters are initialized.
while the solution of state variables does not converge do
    for each phase $l \in \{\mathrm{f},\mathrm{p}\}$ do
        Impose boundary conditions in Eqs. (8) and (9) for velocities $u_l, v_l$
    end for
    Impose the boundary condition in Eq. (10) for the global pressure $\hat{p}$ shared by both phases
    Impose the boundary condition in Eqs. (11) and (12) for the particle volume fraction $\phi_\mathrm{p}$
    for each phase $l \in \{\mathrm{f},\mathrm{p}\}$ do
        Compute the weighting factors $(a_\mathrm{W})_l, (a_\mathrm{E})_l, (a_\mathrm{S})_l, (a_\mathrm{N})_l, (a_\mathrm{P})_l$ in Eqs. (29) and (30)
        Compute the pseudo-velocities $\hat{u}_l$, $\hat{v}_l$ in Eqs. (36) and (37)
    end for
    Compute the weighting factors $b_\mathrm{W}, b_\mathrm{E}, b_\mathrm{S}, b_\mathrm{N}, b_\mathrm{P}$ in the left-hand side of Eq. (44)
    Compute the pseudo-dilation $\hat{\varepsilon}$ in the right-hand side of Eq. (44) for both phases, which expressed by Eq. (43)
    Solve the matrix of the pressure-linked equation (44) with a matrix solver
    Update the pressure $\hat{p}$ with a relaxation factor $\omega_\mathrm{p}$, $\hat{p} \leftarrow (1-\omega_\mathrm{p})\hat{p}^{k-1} + \omega_\mathrm{p}\hat{p}^k$
    Compute the pressure gradients $\frac{\partial \hat{p}}{\partial x}$ and $\frac{\partial \hat{p}}{\partial y}$
    for each phase $l \in \{\mathrm{f},\mathrm{p}\}$ do
        Add the pressure gradients $\frac{\partial \hat{p}}{\partial x}$ and $\frac{\partial \hat{p}}{\partial y}$ to the right-hand side of momentum equations
        Solve the matrix of momentum equations (29) and (30) with a matrix solver
        Update the velocity $u_l$ with a relaxation factor $\omega_\mathrm{v}$, $u_l \leftarrow (1-\omega_\mathrm{v})u_l^{k-1} + \omega_\mathrm{v}u_l^k$
        Update the velocity $v_l$ with a relaxation factor $\omega_\mathrm{v}$, $v_l \leftarrow (1-\omega_\mathrm{v})v_l^{k-1} + \omega_\mathrm{v}v_l^k$
    end for
    Discretize the continuity equation for the particle phase in Eq. (27) with a numerical scheme
    Obtain the particle volume fraction $\phi_\mathrm{p}$ by solving the matrix of the continuity equation (27)
    Obtain $\phi_\mathrm{f}$ with the relationship $\phi_\mathrm{f} + \phi_\mathrm{p} = 1$
    Update the iteration number $k$, $k \leftarrow k + 1$
end while
Return the final solution of state variables of each phase
```

$$= \sum_{l\in\{\mathrm{f},\mathrm{p}\}} \left(\frac{-2\phi_{i,j}\phi_{i+1,j}}{(a_\mathrm{P})_{i,j}\phi_{i+1,j} + \phi_{i,j}(a_\mathrm{P})_{i+1,j}} \right)_l , \tag{47}$$

$$(\kappa_\mathrm{s})_{i,j} = \sum_{l\in\{\mathrm{f},\mathrm{p}\}} \left(\frac{2}{(\kappa_{i,j})^{-1} + (\kappa_{i,j-1})^{-1}} \right)_l$$

$$= \sum_{l\in\{\mathrm{f},\mathrm{p}\}} \left(\frac{-2\phi_{i,j}\phi_{i,j-1}}{(a_\mathrm{P})_{i,j}\phi_{i,j-1} + \phi_{i,j}(a_\mathrm{P})_{i,j-1}} \right)_l , \tag{48}$$

$$(\kappa_\mathrm{n})_{i,j} = \sum_{l\in\{\mathrm{f},\mathrm{p}\}} \left(\frac{2}{(\kappa_{i,j})^{-1} + (\kappa_{i,j+1})^{-1}} \right)_l$$

$$= \sum_{l\in\{\mathrm{f},\mathrm{p}\}} \left(\frac{-2\phi_{i,j}\phi_{i,j+1}}{(a_\mathrm{P})_{i,j}\phi_{i,j+1} + \phi_{i,j}(a_\mathrm{P})_{i,j+1}} \right)_l . \tag{49}$$

Based on the description provided, the steps of the NAPPLE algorithm for particle flow can be summarized as pseudocode in Algorithm 1. For particle flow analysis, we must determine the particle volume fraction by discretizing the particle continuity equation (27) to obtain the linear algebraic equation, which is then solved to find the volume fraction values. The upwind scheme is utilized to discretize the continuity equation of the particle phase.

Besides, the SIS algorithm (Strongly implicit solver) suggested by Lee [84] is utilized for solving the matrices of linear algebraic equations. To ensure numerical stability, the relaxation factors ω_p and ω_v are utilized to update the pressure and velocities for both phases and the values of ω_p and ω_v are set to 0.2 and 0.4 in this study. Moreover, we must iterate the numerical procedure until we achieve solution convergence. The convergence criteria are as follows:

$$\max_{\mathrm{P}} \left| u_{i,j}^k - u_{i,j}^{k-1} \right| \leq \mathrm{tol}_u , \tag{50}$$

$$\max_{\mathrm{P}} \left| v_{i,j}^k - v_{i,j}^{k-1} \right| \leq \mathrm{tol}_v , \tag{51}$$

where tol_u and tol_v represent the convergence criteria for the velocity component u and v for both phases and are set to 1×10^{-5}, respectively.

4.2. Optimization algorithm

In the optimization process, we use a continuation method to progressively increase the projection parameter β in Eq. (16) in each continuation step, which helps to eliminate intermediate design variables. The optimization algorithm iteratively solves the problem based on gradient information during each of these steps. The flowchart of the topology optimization process is shown in Fig. 3.

As shown in Fig. 3, the design variables γ are initialized in the first step. In the second step, the design variables are regularized with the convolution filter in Eq. (14) and the projection function in Eq. (16). We solve the governing equations using the finite difference method in the third step and compute the sensitivities in the fourth step. In the fifth step, we use the GCMMA algorithm to update the design variables [59]. If the objective function does not meet the convergence criterion, the procedure returns to the second step. If it meets the criterion, the procedure verifies whether the continuation steps are completed. If not, the projection parameter β in Eq. (16) is doubled in the next continuation step, and the procedure returns to the second step. Otherwise, the optimization procedure is terminated. The convergence criterion for the objective function is defined as follows:

$$\left| \frac{J_n - J_{n-1}}{J_n} \right| < \epsilon , \tag{52}$$

where ϵ is the criterion for the optimization convergence and is set to 1×10^{-4} in this study.

4.3. Sensitivity analysis based on automatic differentiation

Automatic differentiation offers a robust method for calculating derivatives of functions without the analytical adjoint formulations. Composite functions are decomposed into elementary operations in the process of automatic differentiation. By applying the chain rule to each operation, this approach enables precise computation of derivatives. Therefore, automatic differentiation is well-suited for handling the

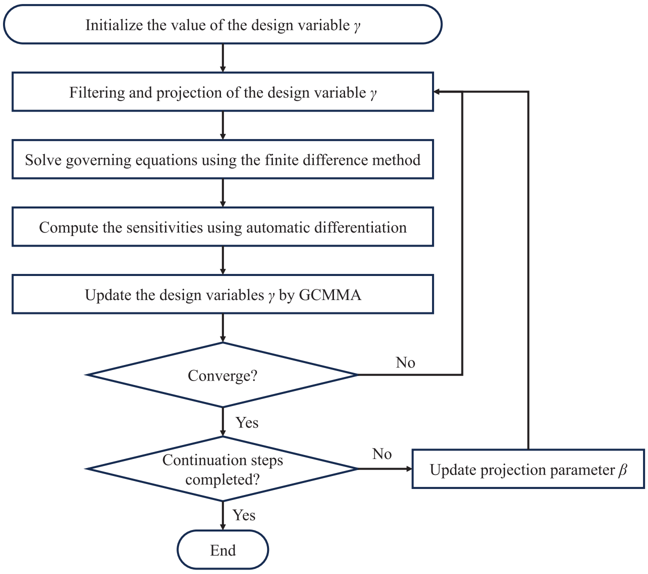

Fig. 3. Flowchart of topology optimization process with a continuation approach of the projection parameter β.

relatively complex equations for particle flow in this study. As reverse differentiation traces the computation backward from the outputs to the inputs, it solves gradient-based optimization problems involving functions with multiple inputs effectively. In this study, we implement the reverse mode automatic differentiation using the library Adept C++ [85]. For sensitivity analysis, it is necessary to declare state variables and related variables as `adouble` objects defined in Adept C++, enabling the tracking of all calculations and the reverse computation of derivatives. To verify the correctness of the sensitivity calculations, the sensitivities obtained from Apept C++ are compared with the results from a finite difference check, as shown in Appendix.

Similar to the iterative solution-based study by Towara and Naumann [86], since the reverse mode automatic differentiation requires recording computational details from each iteration for sensitivity analysis, it significantly increases the memory requirement for the iterative process. To address this issue, we employ a checkpointing algorithm for the sensitivity analysis [63,64]. The operation of a checkpointing algorithm involves dividing the iterative process into several smaller subintervals. At each checkpoint, state variables are recorded and subsequently used to compute adjoint information in reverse, which serves as the initial condition for the next subinterval. As a result, this method significantly reduces memory requirements due to the storage of essential data at these checkpoints and the adjoint calculations within each subinterval.

5. Results and discussion

5.1. Validation of numerical scheme

Using two numerical examples from prior studies [70,87], we validate the feasibility of our numerical scheme. The fluid domain is discretized with a quadrilateral mesh of 160×20. In the first numerical example, the velocity distribution on the central line in a horizontal straight pipe serves as the crucial point, as shown in Fig. 4(a). The fluid phase and particle phase pass through the pipe with a velocity of 1.0 m/s and 0.1 m/s, respectively. Free-slip boundary conditions are applied on the walls. Table 1 shows the relevant physical parameters for this setup. We examine the velocity distribution along the central line of the pipe. As shown in Fig. 5, the numerical results closely match the prior studies. With the increases in particle diameter, a longer distance is required to reach the terminal velocity of particles reasonably.

Table 1
Physical parameters and dimensions for numerical validation.

Parameters	Symbols	Values	Unit
Pipe height	H	4	m
Pipe width	W	0.5	m
Fluid density	ρ_f	1.2	kg/m^3
Particle density	ρ_p	665, 2990	kg/m^3
Particle diameter	d_p	200, 400	μm
Inlet particle volume fraction	ϕ_p^{in}	0.005	–

Table 2
Default physical parameters for the calculation of St_{ref} and the optimization problems.

Parameters	Symbols	Values	Unit
Inlet length	L	0.33	m
Maximum inlet fluid velocity	u_f^{in}	1.0	m/s
Maximum inlet particle velocity	u_p^{in}	1.0	m/s
Fluid density	ρ_f	1.2	kg/m^3
Fluid viscosity	μ	0.04	Pa s
Particle density	ρ_p	1000	kg/m^3
Particle diameter	d_p	1	mm
Inlet particle volume fraction	ϕ_p^{in}	0.005	–

To further validate the flow solver, we consider the effect of gravity. In the second numerical example, the particles driven by the gravity effect flow through a vertical pipe in the quiescent medium, as shown in Fig. 4(b). The velocities of both phases are 0.0001 m/s at the inlet. Free-slip boundary conditions are also applied on the walls. Based on the physical parameters shown in Table 1, the velocity distribution along the central line remains consistent with the prior studies in Fig. 6.

5.2. Particle drag variation maximization problem

5.2.1. Details of numerical setting

In the flow simulation setup, the analysis domains of the two cases are discretized using the quadrilateral meshes of 80×40 and 80×80. In the optimization setting, the initial value of the design variables γ is set to 0.5. The filter radius R is set to 0.05. Additionally, the maximum value of the projection parameter β_{max} and the projection threshold η are set to 32 and 0.5, respectively. For the representation of the solid region, the maximum value of inverse permeability $\overline{\alpha}_f$ is set to 1×10^4, and the convex parameter q is set to 0.02. In the optimization problem, the weighting factors w_Φ and w_ζ in the objective function are set to 0.5, respectively, and the maximum limit of volume constraint $\overline{V}$ is set to $0.5V_0$. It should be noted that c_α is set to St/St_{ref}, where St represents the Stokes number, and St_{ref} corresponds to the Stokes number calculated according to Table 2. The expression of Stokes number is shown as follows:

$$St = \frac{\tau_p}{\tau_f} = \frac{\rho_p d_p^2 U}{18\mu l_o}, \tag{53}$$

where τ_p is the particle relaxation time, τ_f is the characteristic time of the fluid flow, and l_o is the characteristic length of the obstacle. The Stokes number describes the behavior of particles suspended in a fluid flow. It represents the ratio of the particle relaxation time to the characteristic time of the fluid flow, indicating how easily particles can follow the flow. As mentioned in Section 3.2, as the inertia of particles increases, particles tend to follow their original trajectory rather than the fluid flow, which requires applying a larger fictitious body force to prevent particles from penetrating the solid region. Therefore, to properly account for the interaction between particles and the solid region, We set c_α based on the ratio of the Stokes number under different conditions to the reference Stokes number St_{ref}.

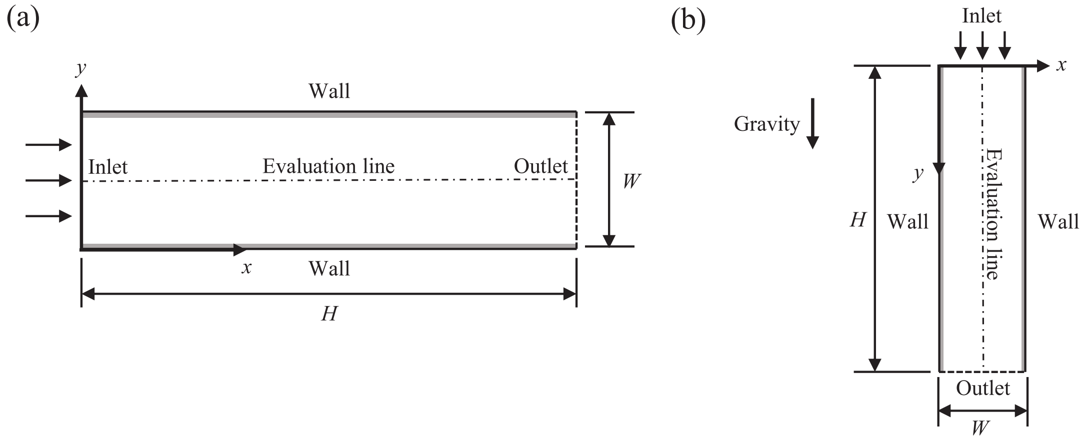

Fig. 4. Dimensions and boundary expressions of analysis domain for numerical validation: (a) Particles flow through a horizontal pipe in the numerical example 1 (b) Particles driven by the gravity effect flow through a vertical pipe in the numerical example 2.

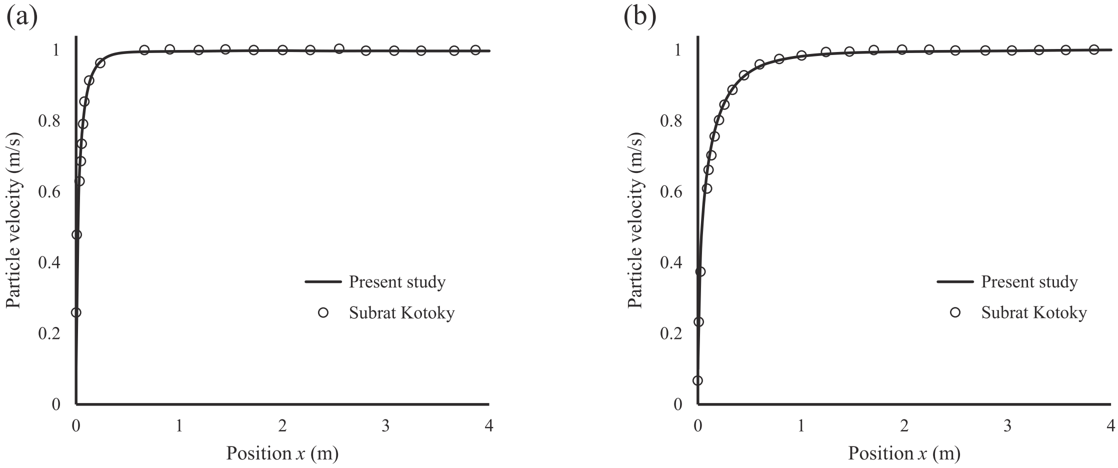

Fig. 5. Comparison of particle velocity distribution along the central line in a horizontal pipe with ρ_p = 665 kg/m^3: (a) d_p = 200 μm (b) d_p = 400 μm.

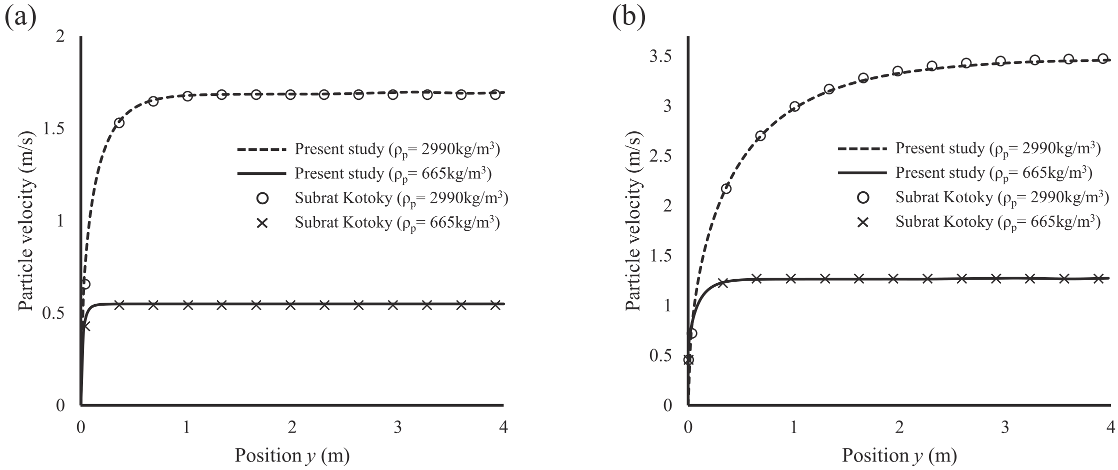

Fig. 6. Comparison of particle velocity distribution along the central line in a vertical pipe: (a) d_p = 200 μm (b) d_p = 400 μm.

5.2.2. Case study 1: symmetrical flow setup

The optimized results are obtained in Fig. 7 according to the parameters in Table 2. The corresponding flow Reynolds number is 10. Fig. 7(a) reveals that the optimized flow field forms a serpentine flow field. From Eqs. (3) and (5), it can be observed that particle drag is primarily influenced by the velocity difference between the particles and the fluid with constant material properties. Since the objective is to enhance the variation of particle drag within the design domain, the velocity difference between the fluid and particles must continuously fluctuate, preventing particles from reaching terminal velocity. In a serpentine flow field, repeated obstructions impede both fluid and particles, and their differing response times create persistent

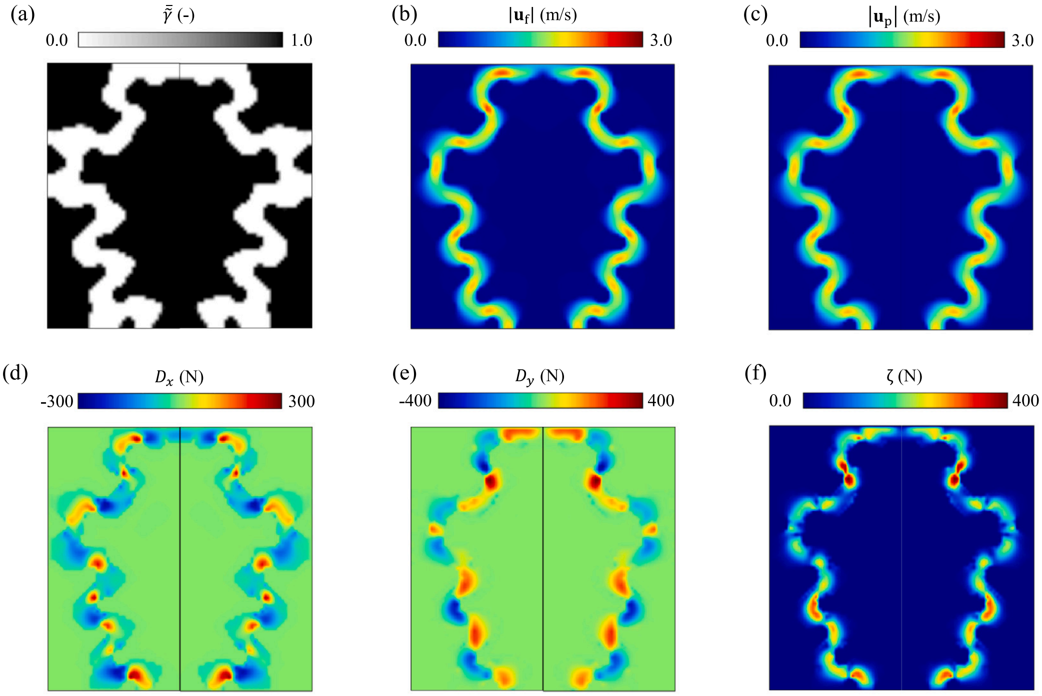

Fig. 7. Distribution of design variables and physical quantities: (a) design variable $\bar{\tilde{\gamma}}$ (b) magnitude of fluid velocity $\mathbf{u}_\mathrm{f}$ (c) magnitude of particle velocity $\mathbf{u}_\mathrm{p}$ (d) magnitude of drag force in the x-direction D_x (e) magnitude of drag force in the y-direction D_y (f) magnitude of particle drag variation ζ.

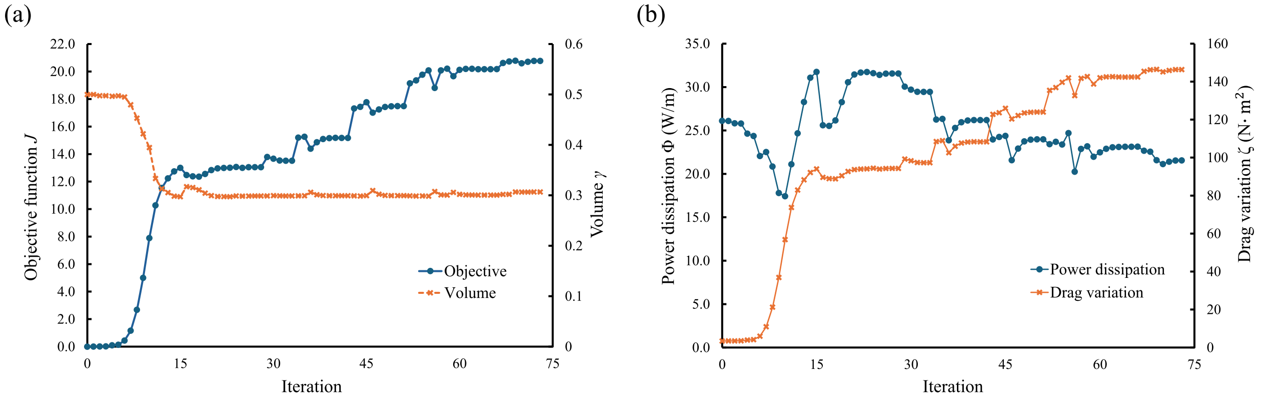

Fig. 8. Convergence history of the optimized flow field in Fig. 7: (a) objective and constraint (b) power dissipation and drag variation.

velocity differences. Consequently, these continuous fluctuations in relative velocity amplify the particle drag variation throughout the design domain.

Fig. 7(b) and (c) demonstrate the distribution of the fluid velocity and particle velocity. Due to the relatively low Stokes number in this case, the particles tend to follow the fluid streamlines closely. Therefore, the distribution of the fluid velocity and particle velocity are nearly identical. However, in Fig. 7(d) and (e), the drag force resulting from the velocity difference between the fluid and the particles is observed. The blue regions indicate areas where the particle velocity exceeds the fluid velocity, while the red regions indicate the opposite. This indicates that particles and fluid undergo acceleration and deceleration in the bends of the serpentine flow field, leading to velocity differences due to their differing response times.

More specifically, as particles enter the bend in the y-direction, due to the obstruction of the bend, the deceleration of the particles in the y-direction is greater than that of the fluid in the red region of Fig. 7(e), while their acceleration in the x-direction exceeds that of the fluid in the blue region of Fig. 7(d). Besides, as particles leave the bend, they continue to accelerate in the y-direction due to inertia and gravity effects. The acceleration of the particles in the y-direction is greater than that of the fluid in the blue region of Fig. 7(e). The repetitive bends of the serpentine flow field increase the flow path length and the number of obstacles in the design domain, leading to greater particle resistance. Fig. 7(f) illustrates the distribution of particle drag variation.

The convergence history is demonstrated in Fig. 8. In addition to satisfying the objective function and constraints, the decrease in power dissipation and the increase in drag variation also indicate that the optimized flow field meets the requirement of increasing the particle resistance while reducing the power dissipation.

Furthermore, we examine the effect of different Reynolds numbers and Stokes numbers on the optimized flow field. In this investigation, the desired value of the Reynolds number is determined by adjusting the viscosity. The optimized flow fields with different Reynolds numbers are shown in Fig. 9. As the Reynolds number increases, the optimized flow field becomes more complex, with an observable

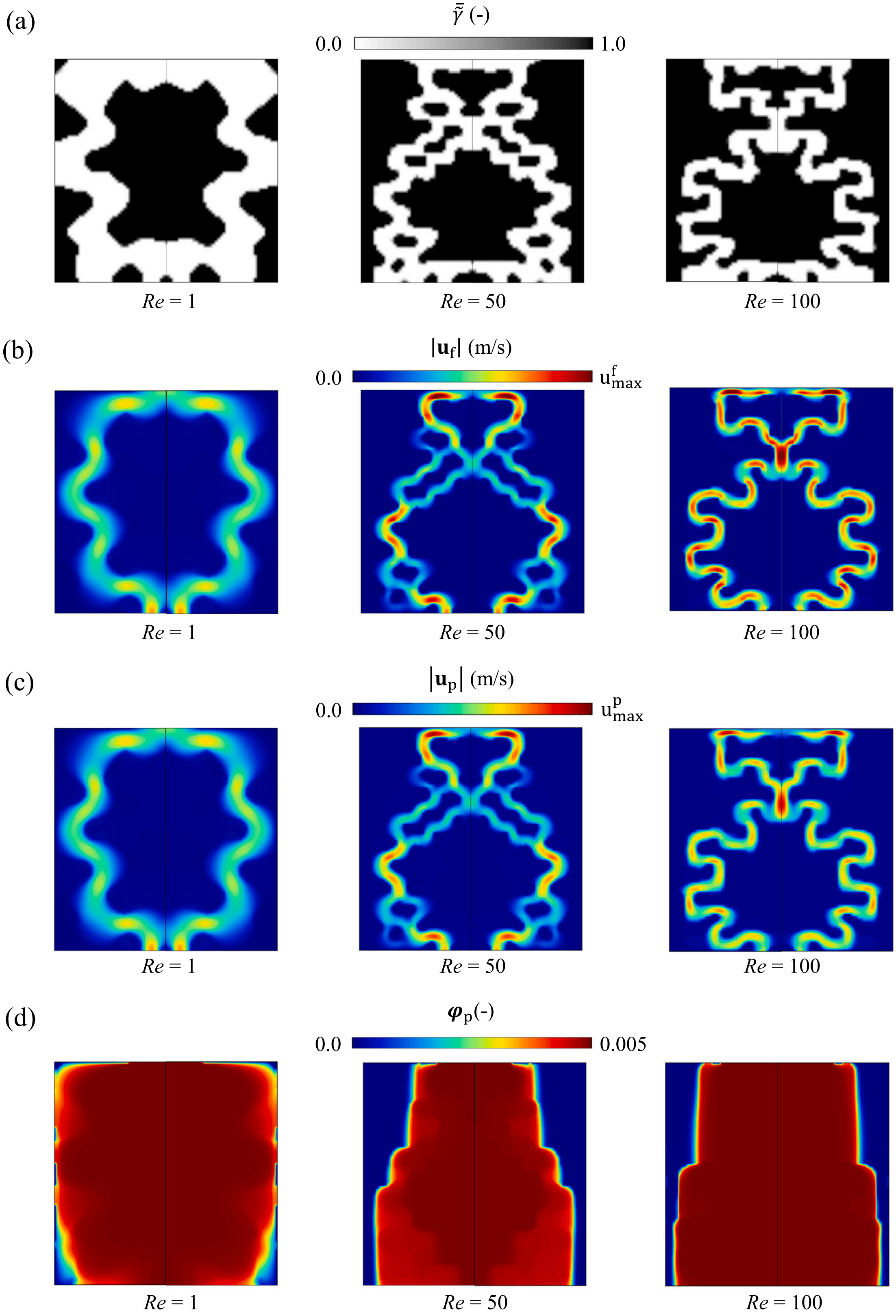

Fig. 9. Optimized Results and physical quantities for different Reynolds numbers: (a) optimized flow field (b) fluid velocity (c) particle velocity (d) particle volume fraction. The maximum values on the color bar for fluid velocity and particle velocity are 2.0 m/s, 3.0 m/s, and 3.5 m/s with *Re* = 1, 50, 100.

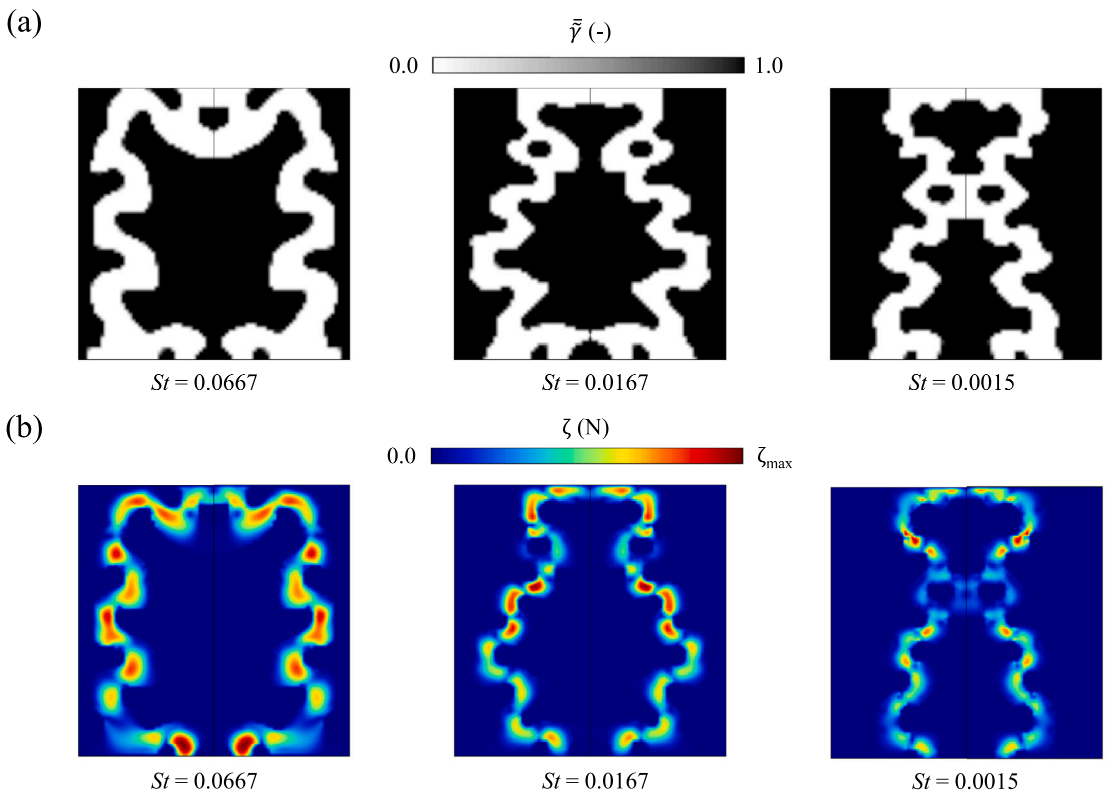

Fig. 10. Optimized results and physical quantities for different Stokes numbers by adjusting the particle diameters to 4 mm, 2 mm, and 0.6 mm: (a) optimized flow field (b) magnitude of particle drag variation. The maximum values of the color bar for drag variation are 155.7, 326.45, and 450.43 with $St = 0.0667$, 0.01667, and 0.0015, respectively.

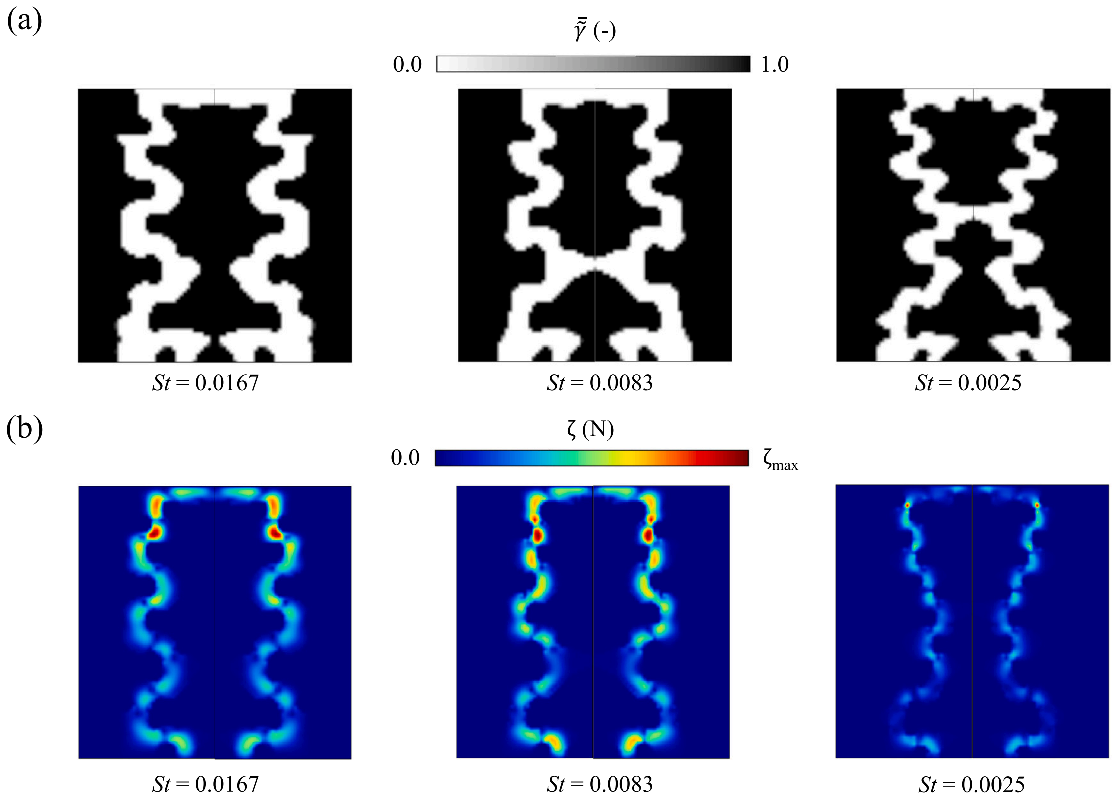

Fig. 11. Optimized flow fields and physical quantities for different Stokes numbers by adjusting the particle densities ρ_p with 4000 $\mathrm{kg/m^3}$, 2000 $\mathrm{kg/m^3}$, and 600 $\mathrm{kg/m^3}$: (a) optimized flow field (b) the magnitude of particle drag variation. The maximum values of the color bar for drag variation are 1814.08, 964.77, 802.42 with St = 0.01667, 0.0083, and 0.0025, respectively.

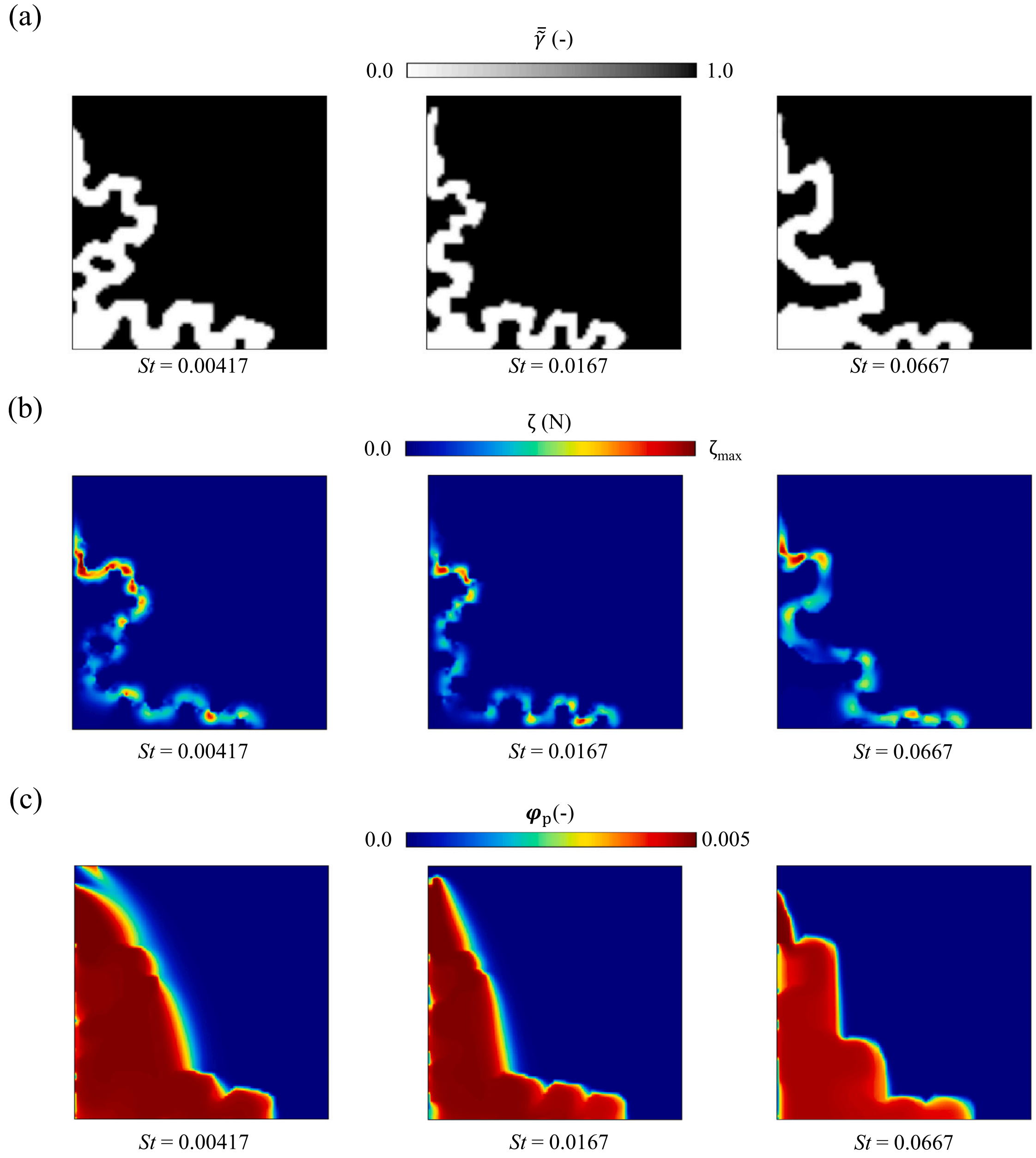

Fig. 12. Optimized Results and physical quantities for different Stokes numbers by adjusting the particle diameters to 1 mm, 2 mm, and 4 mm: (a) optimized flow field (b) magnitude of particle drag variation (c) particle volume fraction. The maximum values of the color bar for drag variation are 980.8, 892.6, and 335.96 with $St = 0.00417$, 0.01667, and 0.0667, respectively.

Table 3
The power dissipation Φ and particle drag variation ζ in J with different Reynolds number using the default parameters in Table 2.

Re	1	10	50	100
Power dissipation Φ (W/m)	58.61	21.56	6.27	11.72
Particle drag variation ζ (N m^2)	44.92	146.38	165.28	272.45

increase in the curvature of the flow channels. Table 3 outlines the power dissipation and particle drag variation with different Reynolds numbers. In the case of a smaller Reynolds number, since viscosity primarily dominates the flow behavior, increasing the drag force by bending the flow channels results in more energy loss. As a result, the number and curvature of bends in the serpentine flow fields are reduced. Moreover, due to the weak inertial effects on the particles, there is a slight difference in the velocity distribution between the particles and the fluid. In the case of a higher Reynolds number, the inertial effects on particles become more significant, resulting in more noticeable differences in the velocity distribution between the particles and the fluid. Particles tend to collide with solids, changing the direction instead of following the fluid streamlines. This behavior increases the degree of variation in drag force.

It should be noted that due to the limitations of the fictitious body force formulation, the particle volume fraction shown in Fig. 9(d) remains within the solid region. Nevertheless, since the fluid velocity and particle velocity inside the solid region are very low, the drag variation within the solid region is also minimal.

Figs. 10 and 11 show the optimized configurations for different Stokes numbers, corresponding to various particle diameters and densities. Generally, the number of bends in the serpentine flow field increases as the Stokes number decreases. On the other hand, regarding bend curvature, a serpentine flow field can be regarded as a sequence of bent pipes, where the characteristic length of a bent pipe l_o is defined

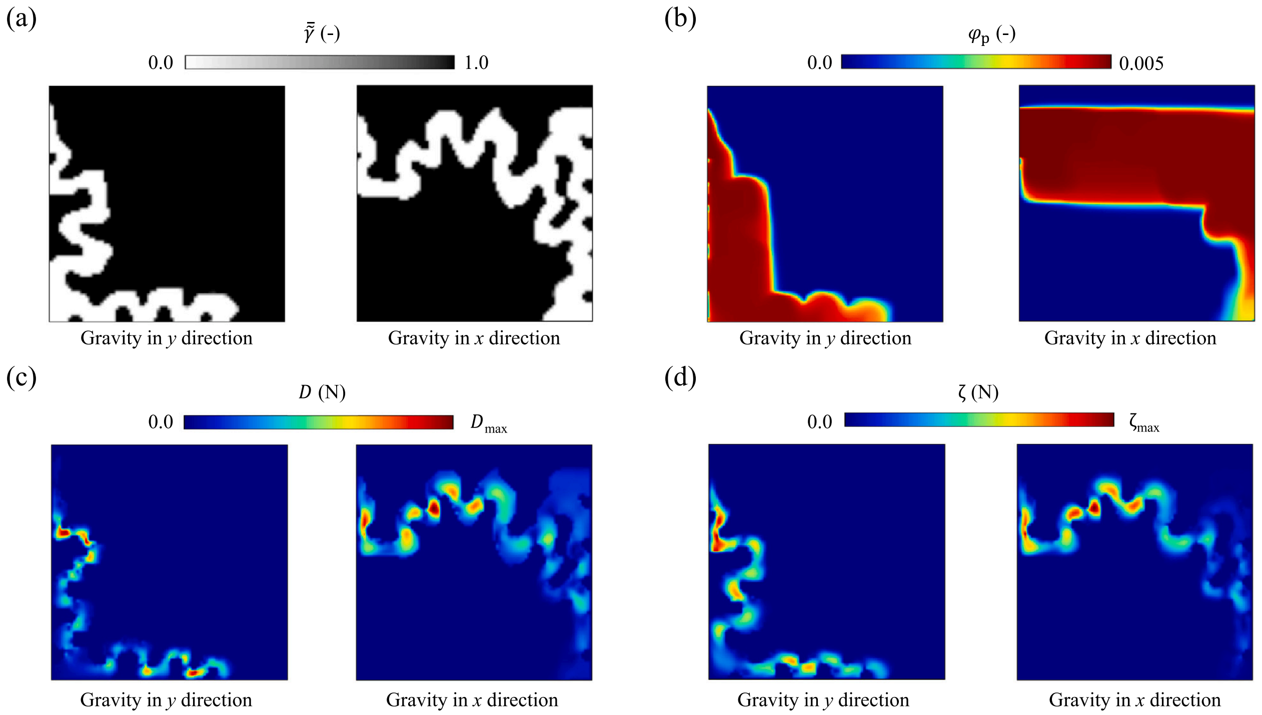

Gravity in y direction Gravity in x direction Gravity in y direction Gravity in x direction

Gravity in y direction Gravity in x direction Gravity in y direction Gravity in x direction

Fig. 13. Optimized Results and physical quantities with $Re = 10$, $d_p = 2$ mm, and $\rho_p = 4000$ kg/m^3: (a) optimized flow field (b) particle volume fraction (c) magnitude of drag force (d) magnitude of particle drag variation. The maximum values of the color bar for drag force are 1362.37 and 1323.49 for gravity in y-direction and x-direction. The maximum values of the color bar for drag variation are 1381.79 and 1244.92 for gravity in y-direction and x-direction.

as its curvature radius R_c [88,89]. As the Stokes number decreases, the overall radius of curvature across all bends in the serpentine flow field decreases.

As the Stokes number decreases, particles follow the fluid streamlines more closely due to the shorter particle relaxation time. Consequently, the optimized flow field requires more bends and smaller curvature radii to enhance variations in the particle drag force. Conversely, as the Stokes number increases, the inertial effects on the particles are enhanced, causing them to adhere more closely to their original trajectories. It becomes easier for particles to detach from the flow streamlines with higher Stokes numbers. In such situations, the influence of bending structures on power dissipation exceeds their effect on particle drag force. The optimized flow field exhibits increased curvature radii and fewer bends to reduce power dissipation.

Tables 4 and 5 outline the power dissipation and particle drag variation with different particle diameters and densities. Reducing particle diameter and density both lead to a decrease in the Stokes number. As mentioned earlier, the number of bends in the flow field increases as the Stokes number decreases. Consequently, reducing particle density and diameter also increases the number of bends, leading to higher power dissipation.

It should be noted that an increase in particle diameter reduces particle drag variation, while an increase in particle density enhances it. This is because particle density also affects gravitational force described in Eq. (3). Although both increasing particle density and diameter cause particles to deviate from fluid streamlines, a higher particle density increases the terminal velocity, thereby amplifying the velocity difference between the particles and the fluid, compared to the effect of increasing particle diameter. As a result, even with a reduction in the number of flow field bends, the enhanced velocity difference leads to an overall increase in particle drag variation with increasing particle density.

Table 4
The power dissipation Φ and particle drag variation ζ in J with different particle diameter using the default parameters in Table 2.

d_p	0.6	1	2	4
Power dissipation Φ (W/m)	19.94	21.56	18.65	13.46
Particle drag variation ζ (N m^2)	137.85	146.38	132.20	93.64

Table 5
The power dissipation Φ and particle drag variation ζ in J with different particle density using the default parameters in Table 2.

ρ_p	600	1000	2000	4000
Power dissipation Φ (W/m)	42.51	21.56	21.75	20.39
Particle drag variation ζ (N m^2)	107.55	146.38	274.41	519.42

5.2.3. Case study 2: asymmetrical flow setup

In this problem setup, we modify the layout of the inlet and outlet to investigate the effect of asymmetric flow on the optimized flow field. The optimization is also based on the parameters in Table 2. Fig. 12 shows the optimized configurations for different Stokes numbers by varying the particle diameter, and the serpentine feature of the flow path remains observable. As the Stokes number increases, both the number of bends and the overall radius of curvature across all bends in the flow field decrease, following the same trend observed in the first problem setting.

Notably, the overall trajectory of the serpentine flow paths in Fig. 12(a) does not follow the shortest route. Instead, they first move downward vertically, then extend toward the outlet on the right. This L-shaped path suggests the presence of gravitational influence on particle movement. Fig. 12(c) shows that the particles tend to flow downward due to the effect of gravity, which explains the L-shaped trajectory of the serpentine flow path.

To further clarify the effect of gravity, Fig. 13 shows the optimized results under different gravity directions. As shown in Fig. 13(a), although the overall trajectory of the serpentine flow path remains L-shaped under different gravity directions, the flow field direction is entirely different. Due to the effect of gravity, the particles move along the direction of gravity, and the resulting distribution of particle volume fraction significantly influences the optimized flow field, as illustrated in Fig. 13(b). When particles are concentrated along the gravity direction, the particle volume fraction in other areas within the design domain becomes low, leading to a reduction in the effect of drag variation in those regions. Consequently, the overall trajectory of the optimized flow field aligns with the particle volume fraction distribution. In Fig. 13(c), the drag distribution represents the velocity difference between the particles and the fluid, which primarily occurs along the serpentine flow path in the direction of gravity. Under the influence of gravity, particles tend to accelerate downward but are repeatedly decelerated as they are obstructed by the serpentine flow path. This continuous cycle of acceleration and deceleration increases the drag variation, as shown in Fig. 13(d). Once the particles descend to the bottom, they can no longer accelerate under gravity, which reduces the velocity difference between the particles and the fluid, and consequently decreases drag variation. Nevertheless, due to the difference in relaxation times between the particles and the fluid, the optimized flow fields still present serpentine flow paths to enhance particle drag variation.

6. Conclusion

In this paper, we proposed a density-based topology optimization method for a particle flow problem with the Eulerian–Eulerian approach. The finite difference method named the NAPPLE algorithm was employed for fluid simulation on a collocated grid. We formulated the optimization problem as a multi-objective function, aiming to maximize the magnitude of particle drag variation while minimizing power dissipation. In the topology optimization framework, automatic differentiation was employed to compute discrete sensitivities without continuous adjoint formulation. The distribution of design variables was obtained via the GCMMA algorithm in the optimization process. For the numerical validation, some numerical examples of one-way coupling particle flow were conducted to compare with the prior works. For the numerical investigation, we considered two cases corresponding to symmetric and asymmetric flow and examined the effects of the Reynolds number, Stokes number, and gravity on the optimized flow field. Our key findings are summarized as follows:

- Flow fields with serpentine features effectively maximize the variation in particle drag force.
- As the Reynolds number increases and the viscous effect decreases, the curvature of bends in the serpentine flow field increases. This enhancement raises the variation in particle drag force.
- With the decrease in the Stokes number, due to the reduced particle relaxation time, the curvature and number of bends in the serpentine flow field increase to raise the variation in particle drag force.
- As the gravitational effect increases, particles concentrate along the direction of gravity, leading the serpentine flow path to align with the particle distribution.

In future work, to extend this method to industrial applications, such as nanofluid applications [90,91] or particle heating receivers [92], it is necessary to incorporate manufacturing constraints and extend the numerical model to dense particle conditions. The parameters such as particle shape, elasticity, and roughness need to be investigated under these conditions. Additionally, the representation of fictitious forces has limitations in fully accounting for the shear stress experienced by particles at the solid walls, which must be addressed.

CRediT authorship contribution statement

Chih-Hsiang Chen: Writing – original draft, Visualization, Validation, Methodology, Investigation, Software, Formal analysis, Data curation, Conceptualization. **Kentaro Yaji:** Writing – review & editing, Supervision, Resources, Project administration, Methodology, Funding acquisition, Conceptualization.

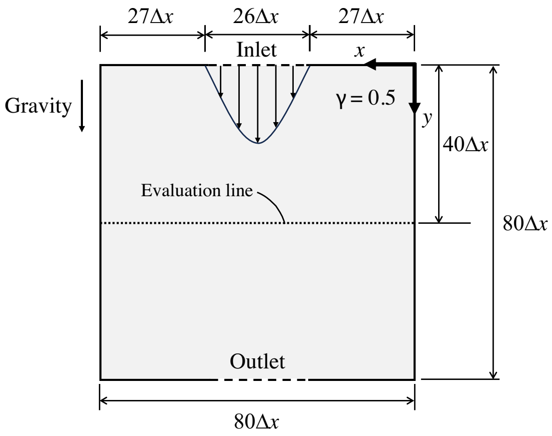

Fig. A.14. A schematic diagram of the evaluation line in the analysis domain to validate discrete sensitivities.

Declaration of competing interest

The authors declare that they have no known competing financial interests or personal relationships that could have appeared to influence the work reported in this paper.

Acknowledgments

This work was supported by JSPS KAKENHI (Grant No. 23H01323).

Appendix. Validation of discrete sensitivities

In this study, we implement automatic differentiation for the sensitivity calculation. To verify the correctness of the sensitivity calculation, we validate the sensitivities with the results of finite difference approximation as follows:

$$\frac{\partial J}{\partial \gamma_k} \approx \frac{J(\boldsymbol{\gamma} + \varepsilon \mathbf{e}_k) - J(\boldsymbol{\gamma})}{\varepsilon}, \tag{A.1}$$

where $\boldsymbol{\gamma} = [\gamma_1\ \gamma_2\ \cdots\ \gamma_n]^\intercal \in \mathbb{R}^n$ is the vector composed of the design variables, $\mathbf{e}_k = [0\ 0\ \cdots\ 1\ 0\ \cdots\ 0]^\intercal \in \mathbb{R}^n$ denotes the standard basis vector whose kth component is 1 while all other components are 0, and ε is a small positive number ranging from $0 < \varepsilon \ll 1$. The sensitivities derived by automatic differentiation should match the outcome obtained by finite difference approximation. Fig. A.14 illustrates the position of the evaluation line in the analysis domain. We examine the sensitivities for the power dissipation Φ and the variation of drag force ζ on the evaluation line separately, corresponding to two cases: $w_\Phi = 1, w_\zeta = 0$ and $w_\Phi = 0, w_\zeta = 1$. The physical parameters for validation are listed in Table 2. As shown in Fig. A.15, the sensitivities obtained from automatic differentiation are entirely consistent with the results from the finite difference approximation.

In addition to the basic finite difference approximation, we further implement the diffuser problem to verify the accuracy of our sensitivity analysis. This problem is often regarded as a benchmark example in topology optimization studies [93–96]. Fig. A.16(a) shows the analysis domain. In this optimization problem, we employ the power dissipation Φ for the objective function and set the maximum value of volume constraint to $0.5V_0$ (V_0 is the volume of the design domain D). The flow Reynolds number is set to 1.0 in the numerical simulation. The velocity boundary conditions for both the inlet and the outlet are parabolic profiles, with the maximum magnitudes set to 1.0 at the inlet and 3.0 at the outlet. Fig. A.16(b) shows the optimized configuration derived through this method, which matches the prior research [28].

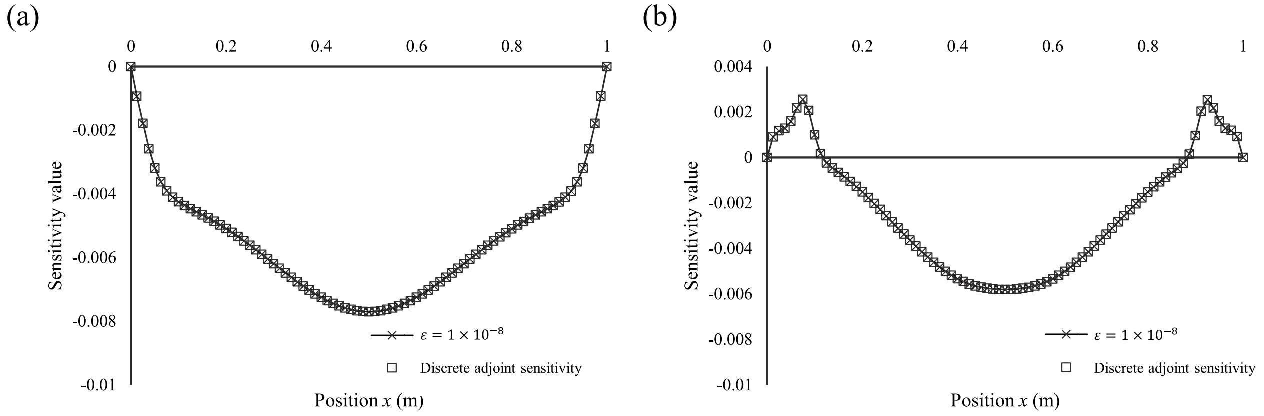

Fig. A.15. Comparison of sensitivities derived by automatic differentiation and finite difference check: (a) power dissipation Φ ($w_\Phi = 1, w_\zeta = 0$) (b) deviation of drag force ζ ($w_\Phi = 0, w_\zeta = 1$).

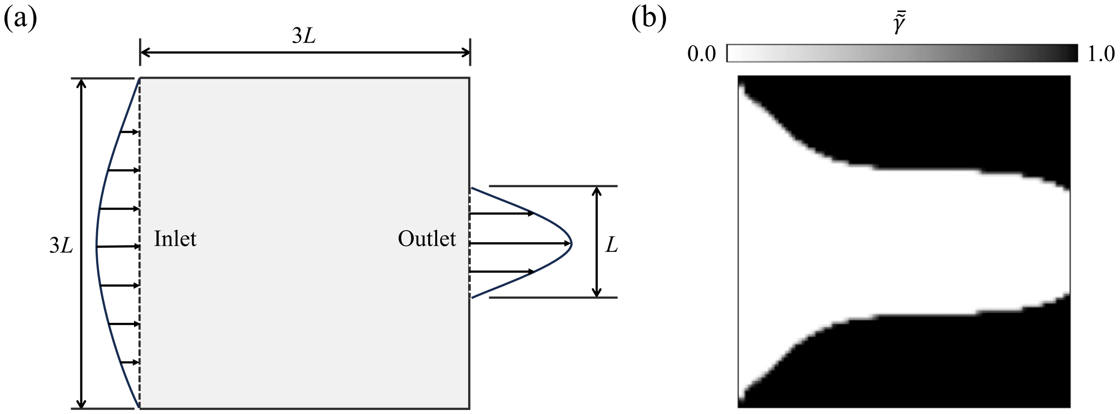

Fig. A.16. Analysis domain and optimized configuration for the diffuser problem: (a) analysis domain (b) optimized configuration.

Data availability

Data will be made available on request.

References

[1] Klaewkla R, Arend M, Hoelderich WF. A review of mass transfer controlling the reaction rate in heterogeneous catalytic systems. Vol. 5, INTECH Open Access Publisher Rijeka; 2011.

[2] Duan H, Wang D, Li Y. Green chemistry for nanoparticle synthesis. Chem Soc Rev 2015;44(16):5778–92.

[3] Duduta M, Ho B, Wood VC, Limthongkul P, Brunini VE, Carter WC, Chiang Y-M. Semi-solid lithium rechargeable flow battery. Adv Energy Mater 2011;1(4):511–6.

[4] Wang H, Lu J. A review on particle size effect in metal-catalyzed heterogeneous reactions. Chin J Chem 2020;38(11):1422–44.

[5] Santana HS, Silva Jr JL, Taranto OP. Development of microreactors applied on biodiesel synthesis: From experimental investigation to numerical approaches. J Ind Eng Chem 2019;69:1–12.

[6] Suh YK, Kang S. A review on mixing in microfluidics. Micromachines 2010;1(3):82–111.

[7] Chaurasia SR, Sarviya R. Thermal performance analysis of CuO/water nanofluid flow in a pipe with single and double strip helical screw tape. Appl Therm Eng 2020;166:114631.

[8] Das SK, Choi SU, Patel HE. Heat transfer in nanofluids—a review. Heat Transf Eng 2006;27(10):3–19.

[9] Hong L, Cheung T-L, Rao N, Ouyang Q, Wang Y, Zeng S, Yang C, Cuong D, Chong PHJ, Liu L, et al. Millifluidic synthesis of cadmium sulfide nanoparticles and their application in bioimaging. RSC Adv 2017;7(58):36819–32.

[10] Kehlenbeck R, Yates JG, Di Felice R, Hofbauer H, Rauch R. Particle residence time and particle mixing in a scaled internal circulating fluidized bed. Ind Eng Chem Res 2002;41(11):2637–45.

[11] Phirommark P, Namchanthra S, Chaiyanupong J, Uapipatanakul S, Chookaew W, Suvanjumrat C, Promtong M. CFD elucidation of microscopic particles in a low-volumetric classifier towards effects of Stokes number and density ratio. Int J Thermofluids 2023;20:100497.

[12] Alhamdan A, Sastry S. Residence time distribution of food and simulated particles in a holding tube. J Food Eng 1997;34(3):271–92.

[13] Lee T, Shin S, Abdel-Khalik SI. Parametric investigation of particulate flow in interconnected porous media for central particle-heating receiver. J Mech Sci Technol 2018;32:1181–6.

[14] Afrin S, Ortega JD, Ho CK, Kumar V. Modeling of a High-Temperature-Serpentine External Tubular Receiver Using Supercritical CO2. In: Energy sustainability. Vol. 45868, American Society of Mechanical Engineers; 2014, V001T02A011.

[15] Al-Ansary H, El-Leathy A, Alswaiyd A, Alaqel S, Saleh N, Saeed R, Al-Suhaibani Z, Danish S, Djajadiwinata E, Jeter S. Study of the optimum discrete structure configuration in obstructed flow particle heating receivers. In: AIP conference proceedings. Vol. 2303, AIP Publishing; 2020.

[16] Bošković D, Loebbecke S, Gross G, Koehler J. Residence time distribution studies in microfluidic mixing structures. Chem Eng Technol 2011;34(3):361–70.

[17] Yang S, Li H, Zhu Q. Experimental study and numerical simulation of baffled bubbling fluidized beds with Geldart A particles in three dimensions. Chem Eng J 2015;259:338–47.

[18] Kreesaeng S, Chalermsinsuwan B, Piumsomboon P. Effect of inserting baffles on the solid particle segregation behavior in fluidized bed reactor: A computational study. ChemEngineering 2024;8(1):7.

[19] Rennebaum HS, Brummerloh DL, Benders S, Penn A. The effect of baffles on the hydrodynamics of a gas-solid fluidized bed studied using real-time magnetic resonance imaging. Powder Technol 2024;432:119114.

[20] An H, Li A, Sasmito AP, Kurnia JC, Jangam SV, Mujumdar AS. Computational fluid dynamics (CFD) analysis of micro-reactor performance: Effect of various configurations. Chem Eng Sci 2012;75:85–95.

[21] Coyle EE, Oelgemöller M. Micro-photochemistry: photochemistry in microstructured reactors. The new photochemistry of the future? Photochem Photobiol Sci 2008;7:1313–22.

[22] Peres JCG, Herrera CdC, Baldochi SL, de Rossi W, dos Santos Vianna Jr A. Analysis of a microreactor for synthesizing nanocrystals by computational fluid dynamics. Can J Chem Eng 2019;97(2):594–603.

[23] Ho CK. A review of high-temperature particle receivers for concentrating solar power. Appl Therm Eng 2016;109:958–69.

[24] Ho CK, Christian JM, Yellowhair JE, Armijo K, Kolb WJ, Jeter S, Golob M, Nguyen C. On-sun performance evaluation of alternative high-temperature falling particle receiver designs. J Sol Energy Eng 2019;141(1):011009.

[25] Aubin J, Prat L, Xuereb C, Gourdon C. Effect of microchannel aspect ratio on residence time distributions and the axial dispersion coefficient. Chem Eng Process: Process Intensif 2009;48(1):554–9.

[26] Bendsøe MP, Kikuchi N. Generating optimal topologies in structural design using a homogenization method. Comput Methods Appl Mech Engrg 1988;71(2):197–224.

[27] Bendsøe MP, Sigmund O. Topology optimization, theory, methods and. 2008.

[28] Borrvall T, Petersson J. Topology optimization of fluids in Stokes flow. Internat J Numer Methods Fluids 2003;41(1):77–107.

[29] Guest JK, Prévost JH. Topology optimization of creeping fluid flows using a Darcy–Stokes finite element. Internat J Numer Methods Engrg 2006;66(3):461–84.

[30] Gersborg-Hansen A, Sigmund O, Haber RB. Topology optimization of channel flow problems. Struct Multidiscip Optim 2005;30:181–92.

[31] Kreissl S, Pingen G, Maute K. Topology optimization for unsteady flow. Internat J Numer Methods Engrg 2011;87(13):1229–53.

[32] Deng Y, Liu Z, Zhang P, Liu Y, Wu Y. Topology optimization of unsteady incompressible Navier–Stokes flows. J Comput Phys 2011;230(17):6688–708.

[33] Yaji K, Yamada T, Kubo S, Izui K, Nishiwaki S. A topology optimization method for a coupled thermal–fluid problem using level set boundary expressions. Int J Heat Mass Transfer 2015;81:878–88.

[34] Yaji K, Yamasaki S, Tsushima S, Suzuki T, Fujita K. Topology optimization for the design of flow fields in a redox flow battery. Struct Multidiscip Optim 2018;57:535–46.

[35] Chen CH, Yaji K, Yamasaki S, Tsushima S, Fujita K. Computational design of flow fields for vanadium redox flow batteries via topology optimization. J Energy Storage 2019;26:100990.

[36] Jenkins N, Maute K. Level set topology optimization of stationary fluid-structure interaction problems. Struct Multidiscip Optim 2015;52:179–95.

[37] Li P, Shi L, Zhao J, Liu B, Yan H, Deng Y, Yin B, Zhou T, Zhu Y. Topology optimization design of a passive two-dimensional micromixer. Chem Phys Lett 2023;821:140445.

[38] Andreasen CS. A framework for topology optimization of inertial microfluidic particle manipulators. Struct Multidiscip Optim 2020;61(6):2481–99.

[39] Yoon GH. Transient sensitivity analysis and topology optimization of particle suspended in transient laminar fluid. Comput Methods Appl Mech Engrg 2022;393:114696.

[40] Yoon GH, So H. Development of topological optimization schemes controlling the trajectories of multiple particles in fluid. Struct Multidiscip Optim 2021;63:2355–73.

[41] Choi YH, Yoon GH. A MATLAB topology optimization code to control the trajectory of particle in fluid. Struct Multidiscip Optim 2023;66(4):91.

[42] Zahari N, Zawawi M, Sidek LM, Mohamad D, Itam Z, Ramli M, Syamsir A, Abas A, Rashid M. Introduction of discrete phase model (DPM) in fluid flow: a review. In: AIP conference proceedings. Vol. 2030, AIP Publishing; 2018.

[43] Balakin BV, Hoffmann AC, Kosinski P, Rhyne LD. Eulerian-Eulerian CFD model for the sedimentation of spherical particles in suspension with high particle concentrations. Eng Appl Comput Fluid Mech 2010;4(1):116–26.

[44] Zhang Y, Ran Z, Jin B, Zhang Y, Zhou C, Sher F. Simulation of particle mixing and separation in multi-component fluidized bed using Eulerian-Eulerian method: A review. Int J Chem React Eng 2019;17(11):20190064.

[45] Gao Y, Muzzio FJ, Ierapetritou MG. A review of the Residence Time Distribution (RTD) applications in solid unit operations. Powder Technol 2012;228:416–23.

[46] Ariyaratne WH, Manjula E, Ratnayake C, Melaaen MC. CFD approaches for modeling gas-solids multiphase flows–a review. In: 9th EUROSIM & the 57th SIMS conference, Oulu. 2016, p. 680–6.

[47] Alexandersen J, Andreasen CS. A review of topology optimisation for fluid-based problems. Fluids 2020;5(1):29.

[48] Yan K, Wang Y, Pan Y, Sun G, Chen J, Cai X, Cheng G. Topology optimization of simplified convective heat transfer problems using the finite volume method. Sci China Technol Sci 2023;66(5):1352–64.

[49] Makhija D, Pingen G, Yang R, Maute K. Topology optimization of multi-component flows using a multi-relaxation time lattice Boltzmann method. Comput & Fluids 2012;67:104–14.

[50] Sasaki Y, Sato Y, Yamada T, Izui K, Nishiwaki S. Topology optimization for fluid flows using the MPS method incorporating the level set method. Comput & Fluids 2019;188:86–101.

[51] Zawawi MH, Saleha A, Salwa A, Hassan N, Zahari NM, Ramli MZ, Muda ZC. A review: Fundamentals of computational fluid dynamics (CFD). In: AIP conference proceedings. Vol. 2030, AIP Publishing; 2018.

[52] Fanxi L, Tianhang X, Xiongqing Y. A fast and automatic full-potential finite volume solver on Cartesian grids for unconventional configurations. Chin J Aeronaut 2017;30(3):951–63.

[53] Barman PC. Introduction to computational fluid dynamics. Int J Inf Sci Comput 2016;3(2):117–20.

[54] Anderson JD, Wendt J. Computational fluid dynamics. Vol. 206, Springer; 1995.

[55] Moukalled F, Mangani L, Darwish M, Moukalled F, Mangani L, Darwish M. The finite volume method. Springer; 2016.

[56] Cheng J, Shu C-W. High order schemes for CFD: A review. Chin J Comput Phys 2009;26(5):633.

[57] Rizzetta DP, Visbal MR, Morgan PE. A high-order compact finite-difference scheme for large-eddy simulation of active flow control. Prog Aerosp Sci 2008;44(6):397–426.

[58] Lee S, Tzong R. Artificial pressure for pressure-linked equation. Int J Heat Mass Transfer 1992;35(10):2705–16.

[59] Svanberg K. A class of globally convergent optimization methods based on conservative convex separable approximations. SIAM J Optim 2002;12:555–73.

[60] Okubo Jr CM, Kiyono CY, Sa LF, Silva EC. Topology optimization applied to 3D rotor flow path design based on the continuous adjoint approach. Comput Math Appl 2021;96:16–30.

[61] Zhao X, Wu B, Li Z, Zhong H. A method for topology optimization of structures under harmonic excitations. Struct Multidiscip Optim 2018;58:475–87.

[62] Farzinazar S, Ren Z, Lim J, Kim JC, Lee J. Thermomechanical topology optimization of three-dimensional heat guiding structures for electronics packaging. J Electron Packag 2022;144(2):021118.

[63] Griewank A, Walther A. Evaluating derivatives: principles and techniques of algorithmic differentiation. SIAM; 2008.

[64] Griewank A, Walther A. Algorithm 799: revolve: an implementation of checkpointing for the reverse or adjoint mode of computational differentiation. ACM Trans Math Softw (TOMS) 2000;26(1):19–45.

[65] Crowe CT, Schwarzkopf JD, Sommerfeld M, Tsuji Y. Multiphase flows with droplets and particles. CRC Press; 2011.

[66] Kim M-C, Klapperich C. A new method for simulating the motion of individual ellipsoidal bacteria in microfluidic devices. Lab A Chip 2010;10(18):2464–71.

[67] Wang Z, Liu C, Wei W. Industry applications of magnetic separation based on nanoparticles: A review. Int J Appl Electromagn Mech 2019;60(2):281–97.

[68] Khashan S, Alazzam A, Furlani E. Computational analysis of enhanced magnetic bioseparation in microfluidic systems with flow-invasive magnetic elements. Sci Rep 2014;4(1):5299.

[69] Sajeesh P, Sen AK. Particle separation and sorting in microfluidic devices: a review. Microfluid Nanofluidics 2014;17:1–52.

[70] Kotoky S. Development and application of a generic finite volume multiphase flow solver for gas particulate flows.

[71] Gidaspow D. Multiphase flow and fluidization: continuum and kinetic theory descriptions. Academic Press; 1994.

[72] Bourdin B. Filters in topology optimization. Internat J Numer Methods Engrg 2001;50(9):2143–58.

[73] Bruns TE, Tortorelli DA. Topology optimization of non-linear elastic structures and compliant mechanisms. Comput Methods Appl Mech Engrg 2001;190(26–27):3443–59.

[74] Diaz A, Sigmund O. Checkerboard patterns in layout optimization. Struct Optim 1995;10:40–5.

[75] Wang F, Lazarov BS, Sigmund O. On projection methods, convergence and robust formulations in topology optimization. Struct Multidiscip Optim 2011;43:767–84.

[76] Prakash C, Patankar S. A control volume-based finite-element method for solving the Navier-Stokes equations using equal-order velocity-pressure interpolation. Numer Heat Transfer 1985;8(3):259–80.

[77] Date A. Complete pressure correction algorithm for solution of incompressible Navier-Stokes equations on a nonstaggered grid. Numer Heat Transfer 1996;29(4):441–58.

[78] Ferziger JH, Perić M, Street RL. Computational methods for fluid dynamics. Springer; 2019.

[79] Shong-Leih L. Weighting function scheme and its application on multidimensional conservation equations. Int J Heat Mass Transfer 1989;32(11):2065–73.

[80] Patankar S. Numerical heat transfer and fluid flow. Taylor & Francis; 2018.

[81] Lee S-L. A new numerical formulation for parabolic differential equations under the consideration of large time steps. Internat J Numer Methods Engrg 1988;26(7):1541–9.

[82] Patankar SV, Spalding DB. A calculation procedure for heat, mass and momentum transfer in three-dimensional parabolic flows. In: Numerical prediction of flow, heat transfer, turbulence and combustion. Elsevier; 1983, p. 54–73.

[83] Moukalled F, Darwish M, Sekar B. A pressure-based algorithm for multi-phase flow at all speeds. J Comput Phys 2003;190(2):550–71.

[84] Lee S-L. A strongly implicit solver for two-dimensional elliptic differential equations. Numer Heat Transfer B 1990;16(2):161–78.

[85] Hogan RJ. Fast reverse-mode automatic differentiation using expression templates in C++. ACM Trans Math Softw (TOMS) 2014;40(4):1–16.

[86] Towara M, Naumann U. A discrete adjoint model for OpenFOAM. Procedia Comput Sci 2013;18:429–38.

[87] Kotoky S, Dalal A, Natarajan G. A parametric study of dispersed laminar gas-particle flows through vertical and horizontal channels. Adv Powder Technol 2018;29(5):1072–84.

[88] Nicolaou L, Zaki T. Characterization of aerosol Stokes number in 90° bends and idealized extrathoracic airways. J Aerosol Sci 2016;102:105–27.

[89] Henríquez Lira S, Torres MJ, Guerra Silva R, Zahr Viñuela J. Numerical characterization of the solid particle accumulation in a turbulent flow through curved pipes by means of stokes numbers. Appl Sci 2021;11(16):7381.

[90] Majeed AH, Mahmood R, Liu D, Zhang Y, Zhang JY, Ren HY, Hendy AS, Ali MR. Effects of oscillation on convective thermal flow in a vertical enclosure filled by nanofluid particles. Case Stud Therm Eng 2024;61:105133.

[91] Majeed AH, Mahmood R, Eldin SM, Saddique I, Saleem S, Jawad M. Natural convection and irreversibility of nanofluid due to inclined magnetohydrodynamics (MHD) filled in a cavity with Y-shape heated fin: FEM computational configuration. CMES Comput Model Eng Sci 2024;139(2).

[92] Hicdurmaz S, Johnson EF, Grobbel J, Amsbeck L, Buck R, Hoffschmidt B. Numerical heat transfer modelling of a centrifugal solar particle receiver. In: AIP conference proceedings. Vol. 2445, AIP Publishing; 2022.

[93] Yaji K, Yamada T, Yoshino M, Matsumoto T, Izui K, Nishiwaki S. Topology optimization in thermal-fluid flow using the lattice Boltzmann method. J Comput Phys 2016;307:355–77.

[94] Xie S, Yaji K, Takahashi T, Isakari H, Yoshino M, Matsumoto T. Topology optimization for incompressible viscous fluid flow using the lattice kinetic scheme. Comput Math Appl 2021;97:251–66.

[95] Suarez MA, Romero JS, Menezes IF. Topology optimization for fluid flow problems using the virtual element method. Mecá Nica Comput 2018;36(45):2037–46.

[96] Padhy RK, Chandrasekhar A, Suresh K. FluTO: Graded multi-scale topology optimization of large contact area fluid-flow devices using neural networks. Eng Comput 2023;1–17.